MICROCOPY RESOLUTION TEST CHART
NATIONAL BUREAU OF STANDARDS-1963-A

⑥

AD-A145 641

CALCULATION OF THE 3-D VISCOUS FLOW AT THE ENDWALL LEADING EDGE REGION OF AN
AXIAL ANNULAR TURBINE CASCADE

Leonard Walitt

Thermo Mechanical Systems Company
Canoga Park, California

DTIC
SEP 1 0 1984
A

DTIC FILE COPY

August 1984

84   9 18   278

TABLE OF CONTENTS

1.0 INTRODUCTION

The principal objective of this research effort is to investigate the feasibility of calculating the roll-up of the endwall boundary layers and subsequent formation of the blade leading edge horseshoe vortices that form at the hub and shroud of a turbine cascade. This investigation is the continuation of a numerical study of the viscous aerodynamics of an annular NASA core turbine cascade described in Reference 1.

The previous viscous aerodynamics cascade study was conducted with the VANS blade-to-blade computer code (Ref. 2). The subsonic turbine cascade flow field was generated in blade-to-blade surfaces. Calculated blade pressures at the hub, mid and tip radii of the cascade agreed with corresponding measurements. However, endwall effects were not included in the blade-to-blade analysis.

Based on the blade-to-blade flow field as the previous approximation, a new meridional computer code was developed to compute endwall effects. The meridional computer code development started from an external aerodynamics code (Ref. 3). This computer code (VANS/MD) numerically solves the equations of motion in a meridional plane which simultaneously intercepts the hub, shroud, and blade of the cascade. Thus, the flow fields at the junctions of the hub and blade and shroud and blade are within the scope of the VANS/MD computer code.

Two important numerical issues are addressed in this report.

1. Applicability of the VANS/MD meridional finite difference equations to unsteady flow.

2. Mass conservation in meridional numerical computation.

The first issue arose because the horseshoe vortices calculated at the blade leading edge were periodic in nature, rather than steady. The second issue deals with the turning of the flow in the meridional computational plane from axial at the upstream boundary to angular at the blade leading edge.

1

In addition to the above numerical issues, background on endwall effects is presented and turbulence modelling is addressed for computation of vortical endwall flow fields. Computations were made for laminar flow and turbulent flow in the NASA core turbine cascade.

Finally, the endwall calculations are presented for the NASA core axial annular turbine cascade. Figure 1 shows top and front views of the NASA core turbine vane annular cascade (Ref. 1). The axial chord is 1.505", there are 36 vanes and the pitch is .174 radians. Flow conditions for the cascade are as follows:

1. $(V/Vcr)_i = .231$

2. $(V/Vcr)_e = .778$

3. $\dot{m} = .3305$ slugs/sec

2.0 SYMBOLS

A Area

C Perimeter of closed curve

C_a Axial chord

C_p Heat capacity at constant pressure

C_v Heat capacity at constant volume ·

E Specific internal energy

H Thermodynamic heat function or enthalpy

h_x Metric of transformation

h_y Metric of transformation

h_z Metric of transformation

$\underline{i}$ Unit vector of curvilinear coordinate x

$\underline{i}_1$ Unit vector of rotating cartesian coordinate of X_1

$\underline{i}_2$ Unit vector of rotating cartesian coordinate of X_2

$\underline{i}_3$ Unit vector of rotating cartesian coordinate of X_3

$\underline{j}$ Unit vector of curvilinear coordinate y

j Index specifying streamlike-lines on a blade-to-blade or meridional surface

k Index specifying potential-like lines on a blade-to-blade or meridional surface

$\underline{k}$ Unit vector of curvilinear coordinate z

M Momentum

$\dot{m}$ Mass flux

n Time index for finite difference equation

P Pressure

r,R Radial coordinate which together with X_3 form a cylindrical coordinate system

S_x Grid velocity component along x direction

S_y Grid velocity component along y direction
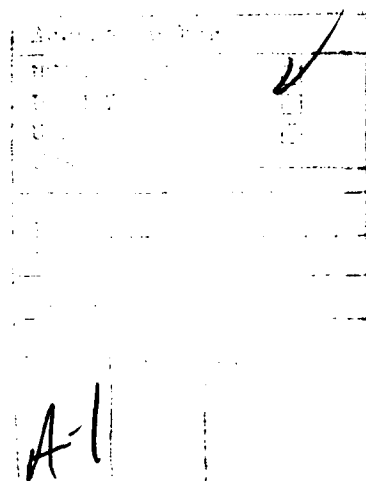
T   Period

t   Time or time-like-variable

u   Velocity component along x direction

$\underline{u}$ Velocity vector

U_z Speed of march along z direction

v   Velocity component along y direction

V   Volume

$\dfrac{V}{V_{cr}}$ Critical velocity ratio

w   Velocity component along z direction

$w'=w-U_z$ Velocity along z on a Galilean Frame which moves with a constant speed U_z along z with respect to the laboratory frame

x   Curvilinear coordinate along Azimuthal direction

X_1 Coordinate axes of rotating Cartesian coordinate which rotate about axial axis X_3 with speed ω

X_2 Coordinate axes of rotating Cartesian coordinate which rotate about axial axis X_3 with speed ω

X_3 Axial coordinate

y   Curvilinear coordinate along streamwise direction (from inlet to discharge)

z   Curvilinear coordinate in marching direction

γ Heat capacity ratio C_p/C_v

δ Boundary layer thickness

ϵ Eddy viscosity

μ Molecular viscosity coefficient

ν Kinematic viscosity coefficient

$\underline{\omega}$ Rotation velocity of impeller

σ_{ij} Total stress tensor

τ_{ij} Reynolds stress tensor

α Angle of attack

β Local flow angle between vane pressure surface and meridional plane

4

ρ Density

τ Characteristic time

τ_w Shearing stress at wall

θ Azimuthal coordinate angle, together with r and X_3 form cylindrical coordinate system

(ξ_1, ξ_2, ξ_3) Curvilinear coordinates

$(\ )_i$ Inlet conditions to cascade

$(\ )_e$ Exit conditions of cascade

$(\ )_r$ Reference condition

$(\tilde{\ })$ Previous approximation property

3.0 BACKGROUND ON ENDWALL EFFECTS

The endwall flow in a turbine cascade is highly three-dimensional and viscous. Langston (Ref. 4) has developed a physical explanation of this endwall phenomenon from measurements. A schematic of the vortical endwall flow, developed by Langston, is shown in Figure 2. At the endwall of the cascade the inlet boundary layer separates and forms a horseshoe (or leading edge) vortex, with one leg of the vortex in one airfoil passage and the other leg in the adjacent passage. A brief description of Langston's physical interpretation of the horseshoe vortex follows.

One leg merges with and becomes part of the passage vortex. Thus in a cascade flow, that part of the secondary flow that is called the passage vortex is an amalgamation of one leg of the horseshoe vortex (and hence part of the inlet boundary layer), the crossflow from the endwall boundary layer formed within the cascade, and entrained fluid from the mainstream flow in the cascade passage.

As shown in Fig. 2, the other leg of the horseshoe vortex, which has been labeled the counter vortex, remains in the suction surface endwall corner. The counter vortex has a sense of rotation opposite to the passage vortex. It is much smaller than the passage vortex and may be dissipated by viscosity.

The ribbon arrow representation of both vortices in Fig. 2 has been drawn to exaggerate the vortex rotation, in order that the sense of rotation of each vortex would be clearly shown. The core of the passage vortex studied approximated a Rankine vortex. A Rankine vortex consists of a circular cylindrical vortex with its axis vertical in a liquid which moves under the action of gravity. The upper surface of this vortex is exposed to atmospheric pressure. A particle of fluid that was near the viscous-inviscid interface of the Rankine vortex would actually have a total gross rotation of one or two revolutions about the center line of the passage vortex, as it passed through the cascade passage.

6

Briley and McDonald (Ref. 5) numerically computed the interaction
of a 2-D wall boundary layer with a single elliptic strut mounted normal
to a flat surface. The flow considered was laminar at very low Mach number,
and resulted in the calculation of a horseshoe-type-vortex. Fig. 3 shows the
strut geometry, coordinate system and representative grid. The equations of
motion were solved in an elliptic-cylindrical coordinate system which fits
all solid surfaces. Planes at constant curvilinear coordinate η (see Fig. 3)
were rotated from the leading edge of the system to the minor axis of the
ellipse. At the symmetry plane of the system these planes are like meridional
planes to the flow, while at the outflow station they become like cross-
sectional planes to the flow. Interactive boundary conditions, derived from
incompressible potential theory and boundary layer theory, were employed along
the inflow elliptical surface. The pressure gradient in the η direction, which
is the driving force for the computation, was derived from potential theory.

Briley and McDonald solved for the flow field for angle-of-attack α of
0 degrees and 5 degrees, respectively. A saddle-point type of flow separation,
i.e., horseshoe vortex, originated upstream of the leading edge and, in the
case of $\alpha = 5^\circ$, toward the high pressure surface of the ellipse. These
results are encouraging, in that a marching method, similar to what is
proposed herein, can compute a horseshoe vortex. However, the vortex was
confined to the immediate vicinity of the elliptic surface due to the single
strut configuration.

Gaugler and Russell (Ref. 6) conducted a large scale test of the NASA core axial annular turbine cascade. From endwall oil traces and streakline flow visualization, the roll-up of the boundary layer and development of the horseshoe vortex was observed. These experiments were conducted over the same Reynolds number range as the small scale axial annular cascade test (Ref. 1); however, the incoming critical velocity ratio of the large scale model was lower than that of the small scale model. Thus, in the leading edge region, where the velocities are small, the simulation between the large and small scale model is good. However, the expansion critical velocity ratio will differ. The endwall oil traces in Fig. 4 show the horseshoe vortex emanating from the pressure surface (Ref. 6).

Finally, NASA has obtained detailed laser velocity measurements for the small scale axial annular turbine cascade model (Ref. 7). These measurements were made at an exit critical velocity ratio of .78. Velocity and flow angles in the blade-to-blade plane were obtained at every 10 percent of axial chord within the passage and at one-half axial chord downstream of the vanes for radial positions near the hub, mean, and tip.

Therefore, the detailed measurements of references 1, 6 and 7 can be employed to evaluate the accuracy of the VANS/MD computations. On the basis of both the experimental and numerical data, the principal fluid mechanics of the endwalls of the system can be resolved. This would represent a major achievement in the computational fluid mechanics of turbomachines.

8

4.0 THE VANS MERIDIONAL COMPUTER CODE

The VANS numerical method (Refs. 2, 8, 9) for turbine cascade flows marches in two alternating directions through the domain of computation. In the blade-to-blade mode of marching (VANS/BB), flow separations along the vane surfaces are computed. The meridional mode of marching (VANS/MD) will calculate hub and shroud effects, including the formation of the horseshoe vortices at the leading edge near the tip and hub endwalls. In addition, VANS/MD can calculate the propagation of the vortex as it moves from the pressure to the suction surface. The blade-to-blade flow field is employed to evaluate source terms in the VANS/MD computer code. Thus, the VANS/BB field is called the previous approximation.

This section addresses three topics:

1. Analogy between the VANS equations and the unsteady equations of motion.

2. Mass conservation for the VANS meridional computer code.

3. Technical approach for computation of endwall effects.

4.1 Analogy Between the VANS Equations and the Unsteady Equations of Motion

An important issue of this study was whether or not the VANS meridional equations were capable of computing unsteady flow. It has been found that in the limit as the angular velocity, U_z, approaches zero, the VANS meridional continuity equation approaches the time-dependent, three-dimensional continuity equation in the meridional plane. A proof of this property of the VANS continuity equation is presented in Appendix A. It follows from the results of Appendix A that the VANS meridional equations reduce to an unsteady set as U_z approaches zero.

4.2 Mass Conservation for the VANS Meridional Computer Code

Figure 5 shows the intersection of a meridional plane with the leading edge. In the case where the flow field is steady, the mass flux entering the upstream boundary must balance the mass flux leaving the face of the

9

meridional plane. No mass can pass through the hub, shroud or blade leading edge.

The continuity equation for a closed curve C of area A in the meridional plane of Figure 5 is as follows (Ref. 2):

$$\frac{d}{dt}\int_{A} \rho\, h_x h_y + \int_{c} \rho(\underline{q} - \underline{q}_s) \cdot \underline{n}\, dC$$

$$- \frac{1}{U_z}\int_{c} \rho w'\, \underline{q}_s \cdot \underline{n}\, dc = -\frac{1}{U_z}\int_{A} \tilde{\rho}\, \tilde{W}'\, h_x h_y\, dA \quad (1)$$

where:

$$\underline{q} = u\, h_y h_z\, \underline{i} + v\, h_x h_z\, \underline{j}$$

$$\underline{q}_s = S_x\, h_x h_y\, \underline{i} + S_y\, h_x h_y\, \underline{j}$$

$$z = U_z\, t$$

$\underline{n}$ = Unit normal to closed curve C

In the case where the curve C corresponds to the meridional boundaries of Figure 5, the second and third terms on the lefthand side of Equation (1) must equal the term of the righthand side of the equation. This follows from the fact that: (a) the flow field is steady; (b) as U_z approaches zero, the VANS continuity Equation (1) approaches the 3-D, time-dependent continuity equation (Appendix A); and (c) only inflow occurs on the boundary C. The pressure gradients of the previous approximation (blade-to-blade solution) were revised to produce a previous approximation angular velocity field which globally preserves continuity (Appendix B). This is similar to global continuity preservation in Spalding's method (Ref. 10). The mass conservative VANS meridional code was then used to run the cascade problem.

For the case of periodically fluctuating conditions, the righthand side of Equation (1) will equal the sum of the second and third terms on the lefthand side after a time average over one period. Thus, this analysis is approximate for periodically fluctuating flow.

10

4.3 Technical Approach for Computation of Endwall Effects

The technical approach for computation of endwall effects, including periodic fluctuations in the flow field, is composed of a blade-to-blade mode of marching followed by a meridional mode of marching. The initial field from which all computation commences is the inviscid MERIDL flow field (Ref. 11). In the blade-to-blade mode of marching, the computation takes place on a blade-to-blade surface which is normal to the meridional planes of the machine, extends from inlet to exit, and moves from the hub to the shroud.

The blade-to-blade method of marching is illustrated in the blade passage schematic shown in Figure 6. The x_1, x_2, and x_3 coordinates of Figure 6 represent a left-handed, rotating, Cartesian coordinate system and coordinates (x, y, z) represent a left-handed, rotating, orthogonal, curvilinear coordinate system. The z-direction is the marching direction with the calculation taking place in the (x,y) blade-to-blade surfaces. The (x,y) blade-to-blade surfaces move from the hub to the shroud of the cascade. The blade-to-blade surface is first coincident with the hub. The velocity U_z is set near zero, i.e., U_z = .20 fps, and the calculation is continued until a steady-state is reached. For the blade-to-blade mode of computation the inlet boundary layer is not present; hence, vortices are not produced. After stabilization at the hub, the blade-to-blade surface is moved to another nearby station; i.e., U_z = 100 fps during the process of going from the initial station to the nearby station. The field is then run to a steady-state in the nearby blade-to-blade surface (U_z = .20 fps). This process is repeated until the entire passage is filled with stabilized blade-to-blade surfaces. For practical purposes approximately ten stabilized blade-to-blade surfaces are desired. This solution represents the first approximation for the meridional mode of computation.

11

In the meridional mode of marching, the meridional plane is first coincident with the vane leading edge. From this position, the plane is then rotated in an angular direction until it intercepts the next vane's suction surface trailing edge. A schematic of two adjacent vane passages with the meridional plane indicated is presented in Fig. 7. The z-direction is now the angular direction. The meridional plane is first coincident with the vane leading edge at its pressure surface (Fig. 5). The angular velocity U_z is set near zero (U_z = .20 rad/sec) and the calculation is continued until a periodic state has occurred. It is anticipated that at least two periods must be computed in this periodic state. After the periodic flow field is obtained at the first station, the meridional plane is moved to a nearby station. The angular velocity is increased to about 100 radians/sec for this purpose. The field is then run to a periodic steady-state in this nearby station. The process is repeated until the entire passage is filled with meridional planes. For practical purposes, approximately ten periodic meridional surfaces are desired.

The blade-to-blade and meridional modes of marching contrast in the boundary conditions that are applied. For the blade-to-blade mode of computation the same boundary conditions are applied throughout the computational process (Ref. 2). However, for the meridional mode of computation the boundary conditions vary (see Section 5.1.3).

5.0 ENDWALL FLOWFIELD CALCULATIONS FOR THE NASA CORE TURBINE CASCADE

In this section the results are presented for turbulent flow in the NASA core turbine cascade. The previous approximation is discussed, as well as meshes, boundary conditions and initial conditions. In addition, the unsteady nature of the vortical flow is described.

5.1 Previous Approximation, Meshes, Boundary Conditions, and Initial Conditions

The calculation completed was that of stabilizing the flow field in the meridional plane intersecting the pressure vane surface at its leading edge (Fig. 5). To this end the angular velocity of the meridional plane U_z was set to the small value of .20 radians/sec for most of the computation.

5.1.1 Previous Approximation

Fig. 8 shows a meridional plane and a blade-to-blade surface. The (x,y) curvilinear coordinate system is shown with the z coordinate being the angular direction. We interpolate the blade-to-blade flow field data (Ref. 2) onto the meridional plane. Each blade-to-blade surface contributes one line of data to each meridional plane. The result is a set of meridional planes containing the blade-to-blade solution. This field becomes the previous approximation to the VANS/MD code, as discussed in Section 4.0.

5.1.2 Finite Difference Meshes

The finite difference mesh on a meridional plane intersecting the pressure vane surface is shown in Fig. 9. The hub, shroud, upstream boundary and cascade vane leading edge are shown. There are 50 vertical lines and 35 horizontal lines. Spacing is fine near the surfaces of the system and coarse away from surfaces. Grid spacing is fine enough to provide about three points in the hub boundary layer at the upstream boundary and seven points in the corresponding shroud boundary layer.

13

5.1.3 Boundary Conditions

The upstream boundary is located 89 percent of an axial chord upstream of the vanes (Fig. 9). The velocity, density and specific internal energy from the blade-to-blade solution are imposed at the upstream boundary. Measured boundary layer velocity profiles are superimposed on the blade-to-blade velocities at the upstream boundary. At the shroud the boundary layer thickness is seven percent of the radial distance between hub and shroud, while on the hub the boundary layer thickness is two percent. It is noted that the boundary layer measurements were taken at an axial chord upstream of the blading; however, they are being employed at the 89 percent chord station for this problem.

A no-slip condition is imposed on the hub, shroud and vane leading edge (Fig. 9).

5.1.4 Initial Conditions and Early Stages of Computation

The interpolated blade-to-blade data (Ref. 2) on the meridional plane intersecting the pressure surface leading edge (Fig. 5) were used as the initial conditions.

The initial angular coordinate was z = -.17453 radians. This angular coordinate will rotate through two pitches, i.e., .348 radians before the solution is completed through the passage.

Figure 10 shows the initial meridional component of the velocity field at a z coordinate of -.17453 radians. The imposed upstream hub and shroud boundary layers are indicated in the figure.

Based on the meridional component of the velocity field of Fig. 10 as the initial condition, the VANS computation commenced at an angular velocity U_z of two radians per second. After 200 cycles[*] of computation the axial velocity components became erratic near the vane leading edge. This behavior was traced to the turbulence

---

[*] A cycle of computation updates all the dependent variables on the mesh in one meridional plane.

model. The Cebeci-Smith mixing length theory (Ref. 12) is not applicable near a stagnation point flow. The turbulence model was gradually shut off starting from 4.4 percent of an axial chord upstream of the vane leading edge. The erratic behavior in the axial velocity field then ceased. The calculation was then run 2400 cycles. The angular coordinate increased by .00237 radians at an angular velocity of two radians per second.

Fig. 11 shows the velocity field after 2400 cycles of computation. Stagnation point flow is indicated at the blade leading edge. In addition, a vortex is seen at the junction of the hub and vane leading edge. However, the rotation of the vortical flow is not correct. The vortex is rotating counterclockwise and should be rotating clockwise (Ref. 4). The problems were traced to the fact that the VANS meridional code was only approximately conserving the passage mass flux. This issue is addressed in Section 4.2 and Appendix B. The VANS/MD computer code was revised to conserve the passage mass flux and the computation commenced with the revised computer code.

5.2 Calculations of Endwall Boundary Layer Roll-up and Vortex Formation.

The VANS mass conservative meridional code was then rerun, in an attempt to stabilize the flow field in the meridional plane intersecting the pressure blade surface leading edge. The meridional plane was initially moved at U_z of two radians per second and then slowed to U_z of .20 radians/sec. The angular coordinate z increased from z = -.1745330 radians to z = -.1660508 radians; i.e., a change of .0085 radians. The meridional plane was moved 4.9 percent of the angular vane pitch.

To define stabilization, the z coordinates were converted to time units, t, through division by the angular velocity U_z. The time variables were then compared to a characteristic time for this problem. The characteristic

time is defined as the time it takes a mid-plane freestream particle to go from the upstream boundary to the vane leading edge. This characteristic time, tc, was determined to be .55 ms. A non-dimensional parameter τ was then defined as:

$$\tau = \frac{t}{tc} \qquad\qquad (2)$$

For the axial cascade problem τ went from zero to 5.44.

A set of velocity vector plots are now presented in terms of the characteristic time parameter τ. These plots depict the transient process of boundary layer roll-up and formation of the horseshoe vortices on the hub and shroud of the system. The meridional component of velocity is plotted.

Figs. 12 to 17 show the velocity field as the characteristic time parameter τ goes from zero to 5.44. At a characteristic time τ = .049 (Fig. 12) a pressure wave is seen moving upstream of the blade leading edge. Fig. 13 at τ = .63, shows the origins of horseshoe vortex formation at the hub and shroud. In addition, a few velocity vectors are parallel to the vane boundary indicating stagnation point flow at the vane leading edge.[*] Figs. 14 through 17 show the development of the hub and shroud horseshoe vortices. At τ = 5.44 these vortices are fully formed (Fig. 17).

Figs. 18, 19 and 20 show critical velocity ratio contour maps at characteristic time parameters of 0.0, 1.93, and 5.44, respectively. In Fig. 20 vortices are indicated in the contour plots and there is a strong viscous flow on the hub and shroud surfaces.

5.3 Unsteady Nature of Vortical Flow Field

The pressure field was inspected from τ = 0 to τ = 5.44, to ascertain whether or not the flow field had stabilized. Table 1 below presents the geometric locations of six points in the meridional plane whose time histories were studied.

---

[*] The meridional flow field breaks up into two paths

16

TABLE 1: GEOMETRIC PROPERTIES OF MESH POINTS WHOSE TIME HISTORIES WERE STUDIED

Point	Axial Position X_3/Ca	Radial Position R/Ca	Description
1	-.62	6.7	Near shroud upstream boundary
2	-.09	6.7	Near shroud vortex
3	-.62	6.2	Near mid-plane upstream boundary
4	-.09	6.2	Near mid-plane at leading edge
5	-.62	5.7	Near hub upstream boundary
6	-.09	5.7	Near hub vortex

The axial position and radial position are in units of axial chord C_a

A raster plot of pressure characteristic time histories is presented in Fig. 21. The ordinate of Fig.21 corresponds to the lower curve $(X_3/C_a = -.62, R/C_a = 6.7)$. Shifting of the ordinate by one-tick-mark makes it applicable to each of the remaining five time histories. On the basis of these data of Fig.21 , it is difficult to determine whether or not the pressure field has stabilized. In order to assess the transient nature of these pressure traces, they were detrended and Fourier analyzed.

Fig. 22 shows raster plots of the mean pressure time histories. A least-square cubic was employed to detrend each of the six pressure traces. The pressure traces near the vortices $(X_3/C_a = -.09, R/C_a = 5.7$ and $X_3/C_a = -.09, R/C_a = 6.7)$ have trends which change significantly; however, they appear near stabilization at $\tau = 5.44$. For points away from the vortical regions, the trend of the data does not significantly change. On balance the trend of the data appears to stabilize for characteristic times greater than $\tau = 3.0$.

Raster plots of the fluctuating part of the pressure-time histories
are presented in Fig. 23. These curves are determined from the difference
between the instantaneous values of Fig. 21 and the detrended values of Fig. 22.
These fluctuating data of Fig. 23 are undersampled in the characteristic time
period of $0 \leq t \leq 5.44$. Thus, it is difficult to determine whether or not
a single frequency persists.

The pressure fluctuations near the eye of the hub vortex have an
amplitude of approximately 100 psf (Fig. 23). This is approximately 5 percent
of the ambient pressure level. Under steady-state conditions this would imply
significant velocity fluctuations. However, due to the unsteadiness in the
flow field, the stagnation enthalpy of the system is itself varying with time.
Thus the total pressure is time-dependent as well. This prevents the velocity
fluctuations from becoming large.

These data of Fig. 23 were Fourier analyzed to determine the power
spectral density in frequency space. Fig. 24 shows raster plots of the power
spectral density of the pressure fluctuations. Plots of spectral density in
units of $(PSFA)^2$/Hz are presented versus $\log_{10}f$. At a value of $\log_{10}f=3.55$
there appears a consistent peak in the power spectral density of all pressure
fluctuations curves; although, the peak is more pronounced in some and less
pronounced in others.

Two numerical experiments were conducted to insure that this periodic
phenomena is not caused numerically. First the marching increment; i.e.,
timestep, was decreased by a factor of two. The VANS code was run 2000 cycles
at this reduced timestep with no change in the periodic nature of the flow field.
Second the angular speed U_z was decreased from two radians/sec to one radian/sec
and then to .20 radians per second. The periodic nature of the flow field was
still unchanged. However, these numerical experiments do not rule out numerical

18

problems. NASA Lewis Research Center will shortly conduct an experiment with high frequency response transducers near the vane leading edge. These measurements will ascertain whether or not the horseshoe vortices are periodic.

The power spectral density curve of Fig. 24 show a maximum level near the eye of the hub vortex and a minimum level near the eye of the shroud vortex. Thus, the hub vortex appears to be the source of the periodicity. Fig. 25 presents plots of the location of the separation point for the hub and shroud horseshoe vortices as a function of calculation time. The amplitude of the hub vortex oscillations appears much greater than the shroud vortex oscillation, although the oscillation frequency appears to be the same. Therefore, the horizontal motion of the hub vortex seems to be the driver for the vortical system.

The meridional flow field was averaged over two periods of the frequency; i.e., $T=\frac{1}{f}=.286$ msec. A velocity vector plot, a critical velocity ratio contour map, and a vorticity ratio contour plot were made of the time-averaged flow field.

Fig. 26 shows the time-averaged velocity field. Boundary layers are present along the hub and shroud. A stagnation point flow is also indicated along the blade leading edge. In addition the vortices do not appear to be the same size. The hub vortex takes up about 16 percent of the radial distance between hub and shroud, while the shroud vortex takes up about 12 percent of this radial distance.

Contours of the critical velocity ratio of the time-average flow field are shown in Fig. 27. Deceleration of the flow from $\frac{V}{Vcr} \approx .23$ to $\frac{V}{Vcr} \approx 0.0$ is clearly seen. In addition the boundary layers and vortices are indicated. Contours similar to this plot, generated downstream of the vane leading edge, can be used to compare with the laser anemometer data of Goldman (Ref. 7).

19

In order to get a more accurate geometric picture of the calculated vortices, contour maps of the vorticity ratio were made in the meridional plane. The vorticity ratio η is defined as:

$$\eta = \frac{1}{\eta_0}\left(\frac{\partial V}{\partial X_3} - \frac{\partial U}{\partial R}\right) \tag{3}$$

where η_0 is a normalization parameter equal to $\eta_0 = U_\infty\left(\frac{1}{\delta_H} - \frac{1}{\delta_S}\right)$, and where U_∞ is the velocity at the upstream boundary, δ_H is the hub boundary layer thickness and δ_S is the shroud boundary layer thickness. The parameter $\eta_0 = 69200$ radians/sec.

Fig.28 shows vorticity ratio contour plots of the time-averaged meridional flow field. The hub vortex has negative vorticity, while the shroud vortex has positive vorticity. Vorticity at the eye of each vortex is about the same; i.e., $\eta \sim 2.0$. However, the vortical shapes are different. The shroud vortex is an oval shape and the hub vortex is more circular. The dividing streamline of the flow between the two vortical regions occurs at a radial position of approximately $R \sim .81$ feet; i.e., $\eta \sim 0$ at $R \sim .81$.

Calculated time-averaged velocity vectors along the hub (axial and angular components) are compared with a photograph of hub endwall oil traces (Ref. 13) in Fig. 29. The vectors in the calculated separation region are not shown in the figure; i.e., they appear as dots. Since the oil traces show only streamline direction, the calculated vectors have been normalized by their magnitudes. Thus, only vector directions emanating from their tails are relevent. The separation point in the figure represents the point at which the meridional vector goes to zero. Upstream of the separation region the calculated vectors are pointed in a direction parallel to the oil trace streamline, and in fact rapidly change direction in the same place as the oil traces. The ratio of the separation point axial distance upstream of the vane to the pitch of the vanes is .267. This compares favorably with the size of the endwall separation region in the oil trace photograph.

20

6.0 TURBULENCE MODELLING AND UNSTEADY VORTICAL FLOW

As was discussed in Section 5.3, the calculated vortical flow field was periodic in nature with a frequency of 3600 Hz. Furthermore, it was found that the Cebeci-Smith turbulence model (Ref. 12) had to be revised in the neighborhood of the blade leading edge (see Section 5.1.4). Thus, an important issue arose, whether or not the turbulence model was the cause of the observed unsteadiness in the calculated flow field.

It was suggested by representatives of NASA Lewis (Ref. 14) that the problem be rerun with the turbulent eddy viscosity set to zero. This calcula- tion is purely a numerical exercise, in that the flow conditions being employed correspond to that of turbulent flow and the turbulence is not included in the calculation. If under these pseudo-laminar conditions unsteadiness still occurred, at least it could not be attributed to the turbulence model employed.

In order to minimize the computational time required for this exercise, it was decided to start the pseudo-laminar computation at a time of 2.42 msec after the start of the turbulent computation. Fig. 30 shows a velocity vector plot of the turbulent meridional flow field at a time of 2.42 msec after the start of computation. This corresponds to a characteristic time of τ of 4.4. This field became the initial conditions for the pseudo-laminar calculation. The eddy viscosity ϵ was set to zero throughout the flow field and the calculation was continued. The pseudo-laminar computation was carried 8000 cycles or to a characteristic time τ of 2.8.

6.1 Pseudo-Laminar Flow Field Structure.

Evolution of the turbulent field of Fig. 30 to a pseudo-laminar field is presented in the velocity vector plots of Figs. 31 to 33. At τ = .346 (Fig. 31) the vortices are starting to get longer and flatter. Fig. 32 (τ=1.55) and Fig. 33 (τ=2.05) clearly show that the vortex pattern has changed shape.

21

A comparison of turbulent and laminar vortical shapes is presented in the vorticity contour ratio plots of Figs. 34 and 35. At τ =.17 (Fig. 34) the flow is essentially turbulent, since the eddy viscosity was just shut off. At τ =2.09 (Fig. 35) the effects of ϵ =0 are quite pronounced. The longer and flatter vortical shapes are clearly indicated.

6.2 Unsteady Nature of Pseudo-Laminar Flow Field

Pressure characteristic time histories were examined at the same six geometric locations employed previously (Table 1).

Fig. 36 shows the pressure characteristic time histories at the six points of Table 1. The flow field appears unsteady; however, it is difficult to tell.

The pressures of Fig. 36 were detrended with a least square cubic fit. The detrended pressure characteristic time histories are shown in Fig. 37. The trend appears to be approaching a constant at a characteristic time τ of 2.8.

The principal issue is whether or not the pressure fluctuations from the detrended values show a persistence of the oscillations. Fig. 38 shows the pressure fluctuations with respect to the detrended values. The oscillations clearly persist.

To demonstrate that a periodic state has occurred, we computed the power spectral density of the pressure fluctuations of Fig. 38. The power spectral density of the pressure fluctuations is shown in Fig. 39. It is clear that a single frequency; i.e., f = 3900 Hz dominates the system. Thus, for the pseudo-laminar case, a periodic state exists at a frequency approximately 300 Hz higher than the turbulent case. Unsteady flow did not attenuate for the pseudo-laminar calculation.

7.0 CONCLUSIONS AND RECOMMENDATIONS

The VANS blade-to-blade and meridional computer codes have been applied to calculate the endwall effects at the NASA core turbine cascade vane leading edge.

The principal conclusions of this study are four-fold:

1. The initial boundary layer roll-up and formation of the endwall vortices were computed at the vane leading edge.

2. The calculated vortical flow field was in a periodic state.

3. The calculated location of the separation point upstream of the vane leading edge for the hub horseshoe vortex was 27 percent of the pitch between vanes which checked closely with endwall oil trace data.

4. The turbulence model has little effect on the periodic nature of the calculated vortical flow field.

It is recommended that the calculation be completed for the NASA core axial annular turbine cascade and the numerical results be compared to existing laser velocimeter data.

8.0 REFERENCES

1.0 Goldman, L. J. and McLallin, K. L., "Cold-Air Annular-Cascade Investigation of Aerodynamic Performance of Core-Engine-Cooled Turbine Vanes I - Solid-Vane Performance & Facility Description", NASA TM X-3224, April, 1975.

2. Walitt, L., "Development of a Locally Mass Flux Conservative Computer Code for Calculating 3-D Viscous Flow in Turbomachines", NASA Contractor Report 3539. April, 1982.

3. Walitt, L.; Liu, C. Y. and Enos, J. A., "A Numerical Method for the Computation of Steady Viscous Flow Fields About Bodies and Angle of Attack," Numerical Continuum Mechanics, Inc. Report, NCMR-79-102, April 1979.

4. Langston, L. S., "Crossflows in a Turbine Cascade Passage," ASME Paper No. 80-GT-5, 5 May 1980.

5. Briley, W. R. and McDonald, H., "Computation of Three-Dimensional Horseshoe Vortex Flow Using the Navier Stokes Equations," Paper at Seventh International Conference on Numerical Methods in Fluid Dynamics, Stanford University and NASA/Ames, June 23-27, 1980.

6. Gaugler, R. E., and Russell, L. M., "Streakline Flow Visualization Study of a Horseshoe Vortex in a Large Scale, Two-Dimensional Turbine Stater Cascade, NASA TM 79274, March 1980.

7. Goldman, L. J. and Seasholtz, R. G., "Laser Anemometer Measurements in an Annular Cascade of Core Turbine Vanes and Comparison with Theory," NASA Technical Paper 2018, June 1982.

8. Walitt, L.; Liu, C. Y.; and Harp, J. L., "An Alternating Direction Explicit Method for Computing Three-Dimensional Viscous Flow Fields in Turbomachines," SAE Paper No. 781001, Vol. 87 of the 1978 SAE Transactions, pp. 3829-3854.

9. Walitt, L., "Numerical Analysis of the Three-Dimensional Viscous Flow Field in a Centrifugal Impeller," AGARD-CCP-282, May 1980.

10. Patankar, S. V. and Spalding, D. B., "A Calculation Procedure for Heat, Mass and Momentum Transfer in Three-Dimensional Parabolic Flows", Int. J. Heat Mass Transfer, Vol, 15, pp. 1787-1806, Permagon Press 1972, Great Britain.

11. Katsanis, T., and McNally, W.D., "Revised FORTRAN Program for Calculating Velocities and Streamlines on the Hub-Shroud Midchannel Stream Surface of an Axial-, Radial-, or Mixed-Flow Turbomachine or Annular Duct," II-Programmer's Manual, NASA TN D-8431, July 1977.

12. Cebeci, T., and Smith, A. M. O. and Mosinskis, G., "Calculations of Compressible Adiabatic Turbulent Boundary Layers", AIAA Journal, Vol. 8, No. 11, p. 1974, 1970.

13. Gaugler, R. E. and Russell, L. M., "Flow Visualization Study of the Horseshoe Vortex in a Turbine Stator Cascade", NASA Technical Paper 1884, June 1982.

14. Private communication from K. Civinskas and L. Povinelli of NASA Lewis Research Center, December 1982.

APPENDIX A

ANALOGY BETWEEN THE VANS EQUATIONS AND THE UNSTEADY EQUATIONS OF MOTION

The VANS meridional computer code equations reduce to the unsteady equations in a fixed meridional plane as the angular speed of the meridional plane approaches zero. In this appendix a proof is given for the continuity equation.

The derivation is developed for the case of a Cartesian coordinate system (x,y,z). Consider the Eulerian, Cartesian coordinate system shown in Fig. 40. Let Γ_1 be a curve in (x,y) plane-1 and let A_1 be the area enclosed.

The three-dimensional, unsteady conservation of mass equation is applied to the area A_1 in (x,y) plane-1. In partial differential form the continuity relation is:

$$\frac{d\rho}{dt} + \frac{d(\rho u)}{dx} + \frac{d(\rho v)}{dy} + \frac{d(\rho w)}{dz} = 0 \qquad (1)$$

Integration of (1) over the area A_1 yields:

$$\frac{d}{dt}\int_{A_1} \rho \, dA + \int_{A_1}\left[\frac{d(\rho u)}{dx} + \frac{d(\rho v)}{dy}\right] dA + \frac{d}{dt}\int_{A_1} \rho w \, dA = 0 \qquad (2)$$

Based on the Gauss Theorem Eqn. (2) can be written as follows:

$$\frac{d}{dt}\int_{A_1} \rho \, dA + \int_{\Gamma_1} \rho \, \underline{q} \cdot \underline{n} \, d\Gamma = -\frac{d}{dt}\int_{A_1} \rho w \, dA \qquad (3)$$

where:

$$\underline{q} = u\underline{i} + v\underline{j}$$

$\underline{n}$ = normal to curve Γ_1 within (x,y) plane-1.

Eqn. (3) can be solved as a function of time in the (x,y) plane, provided the term on the righthand side is known. Let $\tilde{\rho}$ and $\tilde{w}$ represent the

26

density and z-component of velocities, respectively, from a previous approximation.

Then Eqn. (3) can be written as:

$$\frac{d}{dt}\int_{A_1} \rho \, dA + \int_{\Gamma_1} \rho \, \underline{q} \cdot \underline{n} \, d\Gamma = -\frac{d}{dz}\int_{A_1} \bar{\rho} \, \bar{W} \, dA \qquad (4)$$

Eqn. (4) represents the continuity equation for the area A_1 in (x,y) plane-1.

We now consider steady flow for the area A_1 in (x,y) plane-1. The continuity equation is as follows:

$$\frac{\partial(\rho W)}{\partial z} + \frac{\partial(\rho u)}{\partial x} + \frac{\partial(\rho v)}{\partial y} = 0 \qquad (5)$$

Let: $\qquad w = w' + U_z$ \qquad\qquad\qquad\qquad (6)

$\qquad\qquad z = U_z \, \hat{t}$ \qquad\qquad\qquad\qquad\qquad (7)

where U_z is a constant and $\hat{t}$ is a pseudo time-variable. Substitution of (6) and (7) into (5) yields:

$$\frac{\partial \rho}{\partial \hat{t}} + \frac{\partial(\rho u)}{\partial x} + \frac{\partial(\rho v)}{\partial y} = -\frac{\partial}{\partial z}(\rho w') \qquad (8)$$

Integration of (8) with respect to A_1 and use of the Gauss Theorem yields:

$$\frac{d}{d\hat{t}}\int_{A_1} \rho \, dA + \int_{\Gamma_1} \rho \, \underline{q} \cdot \underline{n} \, d\Gamma = -\frac{d}{dz}\int_{A_1} \rho \, w' \, dA \qquad (9)$$

Eqn. (9) can be solved based on the variables $\bar{\rho}$ and $\bar{W'}$ from the previous approximation

$$\frac{d}{d\hat{t}}\int_{A_1} \rho \, dA + \int_{\Gamma_1} \rho \, \underline{q} \cdot \underline{n} \, d\Gamma = -\frac{d}{dz}\int_{A_1} \bar{\rho} \, \bar{W'} \, dA \qquad (10)$$

where: $\qquad\qquad \bar{W'} = \bar{W} - U_z$ \qquad\qquad\qquad (11)

The lefthand side of Eqn. (10) is identical to the lefthand side of Eqn. (4). However, the righthand side terms differ. The righthand side terms of Eqn. (10) represents the change in $\int_{A_1} \bar{\rho} \, \bar{W'} \, dA$ over the interval Δz between (x,y) plane-1 and (x,y) plane-2 in Fig. 40.

We now consider the righthand term of Eqn. (10) and take the limit as U_z approaches zero for a constant $\Delta \overset{n}{t}$; i.e., $\Delta z = U_z \Delta \vec{t}$ approaches zero as U_z appraoches zero. The righthand side of (10) can be written as:

$$\frac{d}{dt} \int_{A_1} \vec{\rho} \, (\vec{W} - U_z) \, dA \cong \frac{\int_{A_2} \vec{\rho}(\vec{W} - U_z) dA - \int_{A_1} \vec{\rho}(\vec{W} - U_z) dA}{U_z \, \Delta \vec{t}} \tag{12}$$

where A_1 and A_2 are defined in Fig. 40. Let us assume that $\vec{\rho}$ and $\vec{W}$ are linear functions of the coordinate z.

$$\left. \begin{array}{l} \vec{\rho} = \vec{\rho}_r + \Delta_\rho \, (z - z_r) \\ \vec{W} = \vec{W}_r + \Delta_w (z - z_r) \end{array} \right\} \tag{13}$$

where: $(\ )_r$ represents a reference value and Δ_ρ and Δ_w represent the constant slopes $\dfrac{d\vec{\rho}}{dz}$ and $\dfrac{d\vec{W}}{dz}$, respectively. The product $\vec{\rho} \, \vec{W}$ becomes

$$\vec{\rho} \, \vec{W} = \vec{\rho}_r \vec{W}_r + \Delta_\rho \Delta_w (z - z_r)^2 + (\Delta_\rho \vec{W}_r + \Delta_w \vec{\rho}_r)(z - z_r) \tag{14}$$

Based on Eqn. (14) the term

$$[\vec{\rho} \, \vec{W} - \vec{\rho} \, U_z]_2 - [\vec{\rho} \, \vec{W} - \vec{\rho} \, U_z]_1 = U_z^2 \left[\Delta_\rho \Delta_w \Delta \vec{t}^2 - \Delta_\rho \Delta \vec{t} \right] + U_z \left[2(z - z_r) \Delta \vec{t} \, \Delta_\rho \Delta_w + \vec{W}_r \Delta_\rho \Delta \vec{t} + \vec{\rho}_r \Delta_w \Delta \vec{t} \right] \tag{15}$$

Now, if it is assumed that the area A_1 is identical to the area A_2, then the righthand side of Eqn. (12) can be written for a small area element ΔA as follows:

$$\frac{\left\{ [\vec{\rho} \vec{W} - \vec{\rho} U_z]_2 - [\vec{\rho} \vec{W} - \vec{\rho} U_z]_1 \right\} \Delta A}{U_z \, \Delta \vec{t}} = \left\{ U_z^2 (\Delta_\rho \Delta_w \Delta \vec{t}^2 - \Delta_\rho \Delta \vec{t}) \right. $$
$$\left. + U_z \left(2(z_1 - z_r) \Delta t \, \Delta_\rho \Delta_w + \vec{W}_r \Delta_\rho \Delta \vec{t} + \vec{\rho}_r \Delta_w \Delta \vec{t} \right) \right\} \frac{\Delta A}{U_z \Delta \vec{t}} \tag{16}$$

Taking the limit of Eqn. (16) as $U_z \longrightarrow 0$ yields:

$$\lim_{U_z \to 0} \frac{\left\{ [\tilde{\rho}\tilde{W} - \tilde{\rho}U_z]_2 - [\tilde{\rho}\tilde{W} - \tilde{\rho}U_z]_1 \right\} \Delta A}{U_z \Delta \tilde{t}} = \left\{ \Delta\rho\,(\tilde{W}_r + \Delta_W\,(z_1 - z_r)) \right.$$
$$\left. + \Delta_W\,(\tilde{\rho}_r + \Delta\rho\,(z_1 - z_r)) \right\} \Delta A \qquad (17)$$

Based on Eqn. (13) the final result becomes:

$$\lim_{U_z \to 0} \frac{\left\{ [\tilde{\rho}\tilde{W} - \tilde{\rho}U_z]_2 - [\tilde{\rho}\tilde{W} - \tilde{\rho}U_z]_1 \right\} \Delta A}{U_z \Delta \tilde{t}} = \left\{ \Delta\rho\,\tilde{W}_1 + \Delta_W\,\tilde{\rho}_1 \right\}$$
$$= \left\{ (\frac{\partial \tilde{\rho}}{\partial z})\tilde{W}_1 + (\frac{\partial \tilde{W}}{\partial z})\tilde{\rho}_1 \right\} \qquad (18)$$

Integration of (18) over the area A_1 yields:

$$\lim_{U_z \to 0} \left[-\frac{d}{dz} \int_{A_1} \tilde{\rho}\,\tilde{W}'\,dA \right] = -\frac{d}{dz} \int_{A_1} \tilde{\rho}\,\tilde{W}\,dA \qquad (19)$$

where differentiation and integration have been reversed.

Therefore, on the basis of Eqn. (19), the VANS continuity equation reduces to the unsteady Eqn. (4) in the limit as U_z approaches zero.

APPENDIX B

MASS CONSERVATION FOR THE MERIDIONAL COMPUTER CODE

In order to preserve continuity the VANS meridional finite difference equations were revised. The analysis is presented herein.

Consider the finite difference mesh of Fig. 9. The horizontal lines are labelled by the coordinate k and the vertical lines are labelled by the coordinate j. Since no slip flow is imposed at the hub, shroud and blade leading edge of the system, the mass flux entering at the upstream boundary must equal the change in mass within the meridional plane plus the mass flux leaving the face of the meridional plane. Under steady state conditions the mass does not change within the meridional plane; thus, the incoming mass flux must equal the mass flux leaving the meridional plane face.

Eqn. (1) of Section 4.2 can be expressed in finite difference form for the entire mesh. The relation is as follows:

$$\frac{SMASSI^n - SMASSI^{n-1}}{\Delta t} = -SMSTPT^{n-\frac{1}{2}} + \frac{CCTERM^{n-\frac{1}{2}}}{\Delta t} \tag{1}$$

where: SMASSI is the sum of the masses of all the zones of the mesh

SMSTPT is the mass transort through the boundaries of the system (in this case only the incoming flux).

CCTERM is the mass flux passing through the meridional plane face (based on conditions from the previous iteration).

n is the cycle count corresponding to the time t^n.

n-1 is the cycle count corresponding to the time t^{n-1}

The parameter CCTERM can be written as a summation of individual fluxes as follows:

$$CCTERM^{n-\frac{1}{2}} = \sum_{k=1}^{k_t} \sum_{j=1}^{j_r} CTERMS^{n-\frac{1}{2}} (j,k) \tag{2}$$

where:

$$k_t = k_{MAX} - 1$$
$$j_r = j_{MAX} - 1$$

The expression CTERMS (j,k) can be written as follows:

$$CTERMS^{n-\frac{1}{2}}(j,k) = \frac{1}{4U_z}\left\{ \bar{\rho}^n_{jk} V^n_{jk}\left[\sum_{i=1}^{4} h^n_{x_i} h^n_{y_i}(U_z - \widehat{W}^n_i)\right]_{j,k} \right.$$
$$\left. - \bar{\rho}^n_{jk} V^{n-1}_{jk}\left[\sum_{i=1}^{4} h^{n-1}_{x_i} h^{n-1}_{y_i}(U_z - \widehat{W}^{n-1}_i)\right]_{jk} \right\} \qquad (3)$$

where: ($\smallsmile$) represents a previous approximate variable

$\displaystyle\sum_{i=1}^{4}[\qquad]$ represents a summation over a single zone of the mesh of
Fig. 9.

We now let the angular velocities $\widehat{W}_i$ be defined as follows:

$$\widehat{W}_i = \widehat{\widehat{W}}_i + W_c \qquad (4)$$

where: W_c is independent of the particular zone in question.

Combining (3) and (4) yields:

$$CTERMS (j,k) = \frac{1}{4U_z}\left\{ \bar{\rho}^n_{jk} V^n_{jk}\left[\sum_{i=1}^{4} h^n_{x_i} h^n_{y_i}(U_z - \widehat{\widehat{W}}^n_i)\right]_{jk} \right.$$
$$\left. - \bar{\rho}^{n-1}_{jk} V^{n-1}_{jk}\left[\sum_{i=1}^{4} h^{n-1}_{x_i} h^{n-1}_{y_i}(U_z - \widehat{\widehat{W}}^{n-1}_i)\right]_{jk} \right\}$$
$$- \frac{1}{4U_z}\left\{ W^n_c \bar{\rho}^n_{jk} V^n_{jk}\left[\sum_{i=1}^{4} h^n_{x_i} h^n_{y_i}\right]_{jk} - W^{n-1}_c \bar{\rho}^{n-1}_{jk} V^{n-1}_{jk}\left[\sum_{i=1}^{4} h^{n-1}_{x_i} h^{n-1}_{y_i}\right]_{jk} \right\} (5)$$

If we substitute Eqn. (5) into Eqn. (1) and set the righthand side of
Eqn. (1) to zero, we can solve for $W_c{}^n$. The expression for $W_c{}^n$ is as follows:

$$W_c{}^n = \left[\frac{W_c{}^{n-1} ZMASS^{n-1}}{U_z} - DEWBAR\right]\left(\frac{U_z}{ZMASS^n}\right) \qquad (6)$$

31

where:

$$DEWBAR = (\Delta t) SMSTPT^{n-\frac{1}{2}} - \frac{1}{4 U_z} \sum_{k=1}^{k_t} \sum_{j=1}^{j_r} \left\{ \bar{\rho}_{jk}^n V_{jk}^n \left[\sum_{i=1}^{4} h_{x_i}^n h_{y_i}^n (U_z - \bar{\bar{W}}_i^n) \right]_{jk} \right.$$

$$\left. - \bar{\rho}_{jk}^{n-1} V_{jk}^{n-1} \left[\sum_{i=1}^{4} h_{x_i}^{n-1} h_{y_i}^{n-1} (U_z - \bar{\bar{W}}_i^{n-1}) \right]_{jk} \right\}$$

$$ZMASS^n = \sum_{k=1}^{k_t} \sum_{j=1}^{j_b} \bar{\rho}_{jk}^n V_{jk}^n \left[\sum_{i=1}^{4} h_{x_i}^n h_{y_i}^n \right]_{jk}$$

$$ZMASS^{n-1} = \sum_{k=1}^{k_t} \sum_{j=1}^{j_r} \bar{\rho}_{jk}^{n-1} V_{jk}^{n-1} \left[\sum_{i=1}^{4} h_{x_i}^{n-1} h_{y_i}^{n-1} \right]_{jk}$$

Therefore, we have found a velocity W_c^n at each cycle n for which the mass flux about the exterior boundaries of the mesh of Fig. 9 will equal the total mass flux leaving the face of the system. The angular pressure gradient in the z momentum equation is adjusted to produce the angular velocity increment W_c^n at each cycle of computation. Thus, the mass flux globally entering the system at its upstream boundary is equal to that leaving the face of the meridional plane. It is noted that the velocity W_c^n turns out to be a small fraction of the angular velocity $\bar{\bar{W}}_i^n$ calculated from the z momentum equation.

For the case of periodic steady-state conditions, the righthand side of Eqn. (1) will be zero after a time average over one period. Thus, for the case of periodic steady flow the analysis herein is approximate.

32

APPENDIX C

BOUNDARY CONDITIONS FOR MERIDIONAL MODE OF MARCHING

In this section the boundary conditions are described as the meridional plane rotates through a blade passage. The rotation phase of the computation will be conducted in a future effort.

The hub blade-to-blade surface is shown in Fig. 41. The domain of computation starts approximately 90 percent of an axial chord upstream of the blade leading edge. Locations for eleven calculational meridional planes are shown in Fig. 41. The viscous flow field on meridional calculational plane "1" has already been computed (see Section 5.1.3 for boundary conditions).

Boundary conditions appropriate to the eleven meridional calculational planes of Fig. 41 are described. Boundary conditions for planes 2 to 6 are identical to those of plane 1. Plane 6' is divided into two parts. The upstream part has boundary conditions similar to plane 6. A no slip flow boundary condition is applied on the boundaries of the downstream part of calculational plane 6' and plane 7. No slip flow is imposed on the upstream boundary, hub and shroud of meridional calculation planes 8 and 9, while periodic conditions are specified at the downstream boundary of these planes. Meridional calculational planes 10 and 11 maintain no slip flow at their upstream boundaries, hub, and shroud. A pressure boundary condition is imposed at the downstream boundary of these meridional planes. It is noted that near the vane trailing edge the meridional calculational planes of Fig. 41 define the cross-sectional flow field more accurately than a set of cross-sectional surfaces normal to the axis.

33

meridional plane at suction surface leading edge

meridional plane at pressure surface leading edge

Flow

Test vanes

Station 1

3.6 cm (1.5 in.)

Station 2 (vane trailing edge)

Station 3 (survey plane)

Middle test vane wake

1.3 cm (0.5 in.)

10.2 cm (4.0 in.)

Station 3M (after mixed conditions)

(a) top view

Vane trailing-edge

θ

meridional plane at pressure surface leading edge

meridional plane at suction surface leading edge

(b) front view

Fig. 1: Schematic of turbine cascade showing meridional planes of computation; θ defines the angular coordinate of the meridional plane.
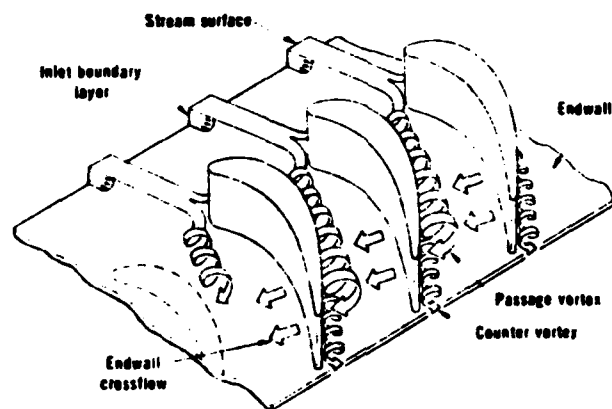
Fig. 2. The three-dimensional separation of a boundary layer entering a turbine cascade. The saddle point occurs where the vortex is formed

35
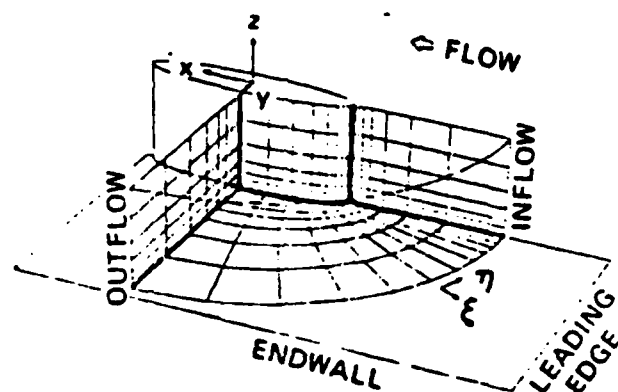
Fig. 3- Geometry, Coordinate System, and Representative Grid
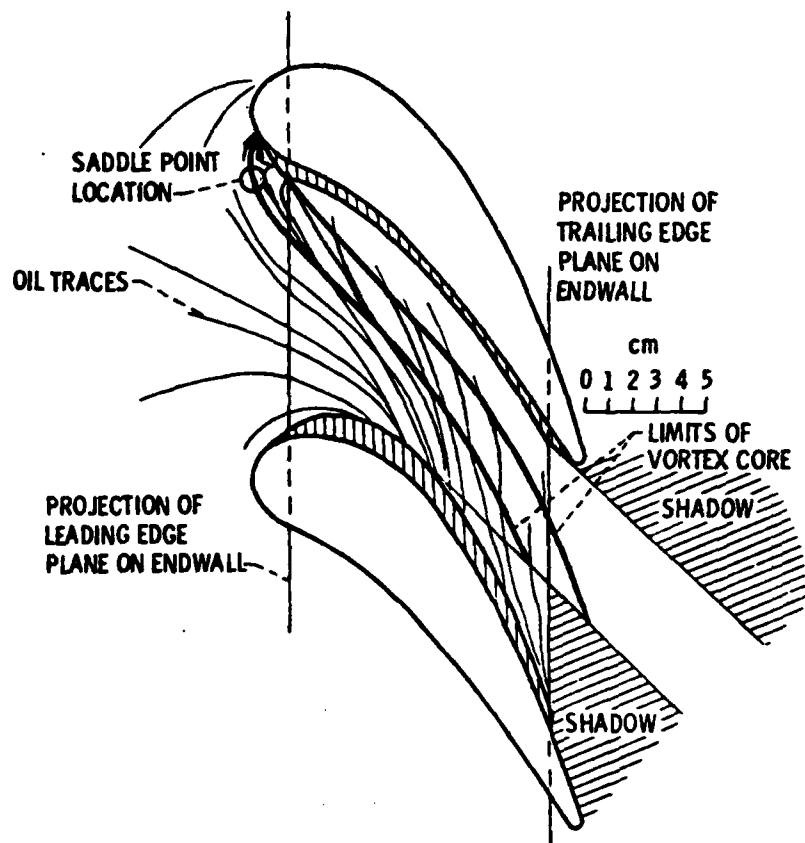
Figure 4 - Location of vortex superimposed on endwall oil traces.
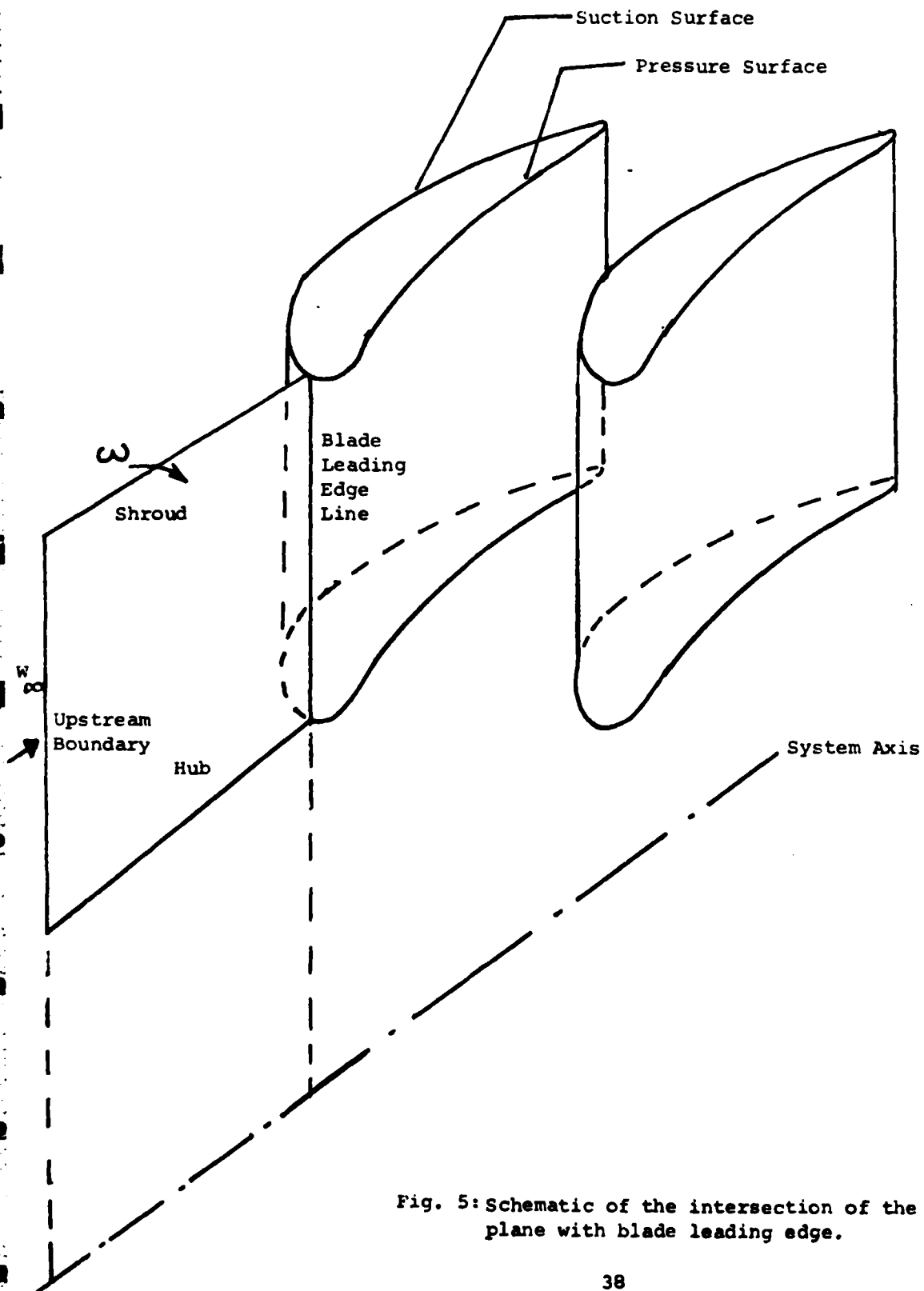
Fig. 5: Schematic of the intersection of the meridional calculational plane with blade leading edge.
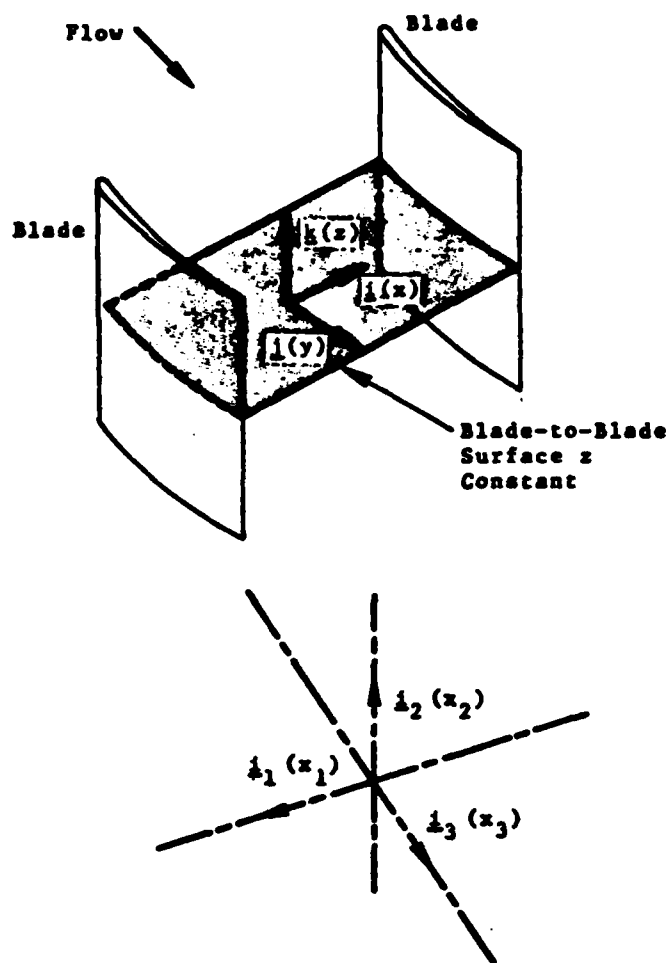
Fig. 6 – Schematic of cascade blading passage illustrating
the blade-to-blade mode of marching.
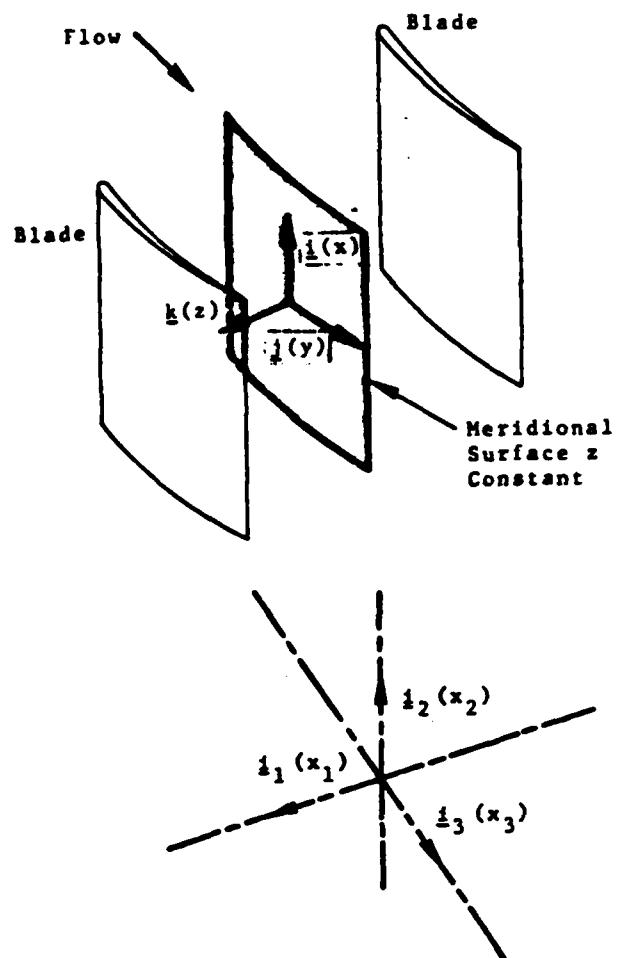
Fig. 7 - Schematic of cascade blading passage illustrating
meridional mode of marching.
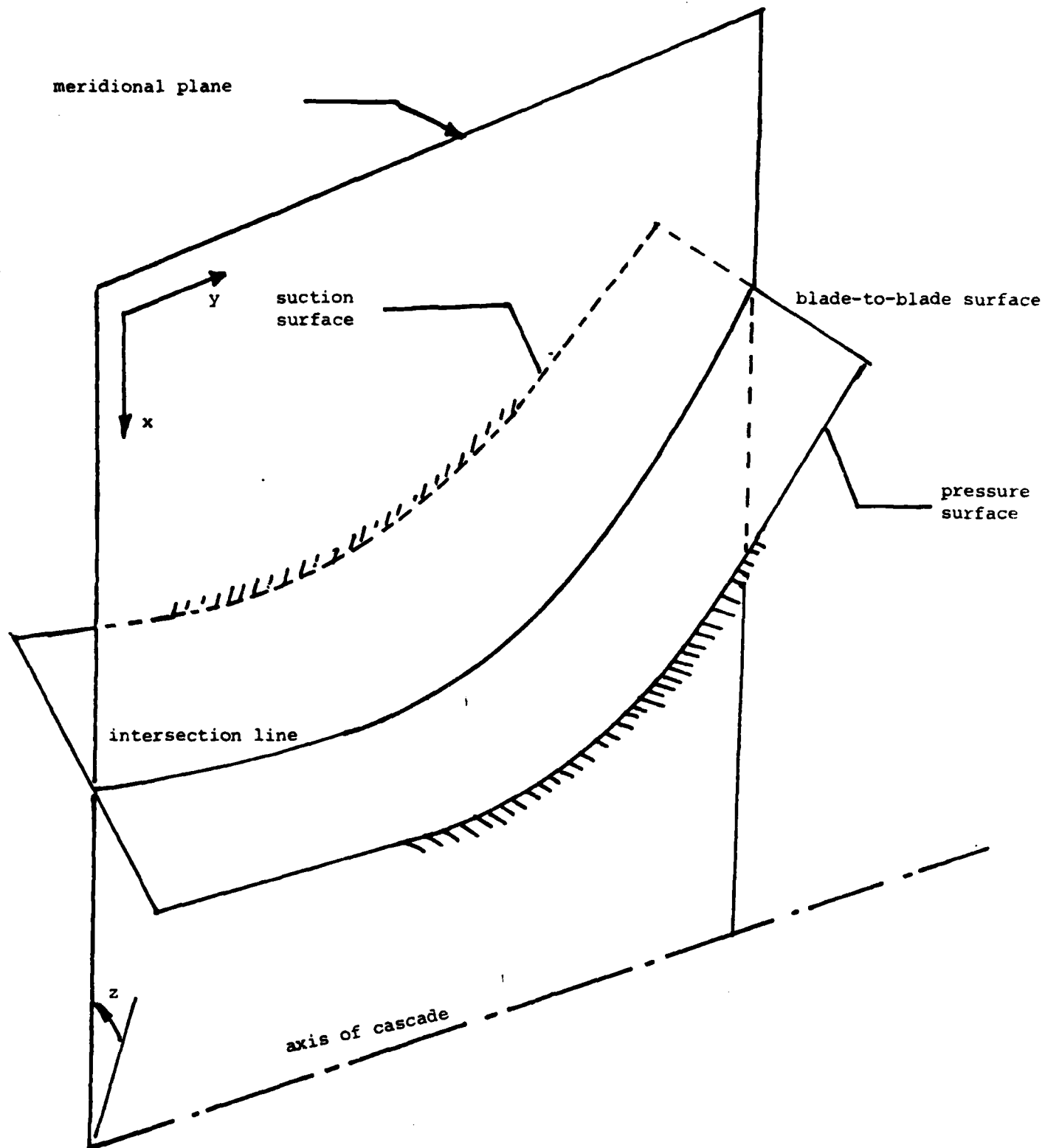
Figure 8. Schematic of the intersection of a meridional plane with a cascade blade-to-blade surface; cross hatched areas indicate blade surface regions.
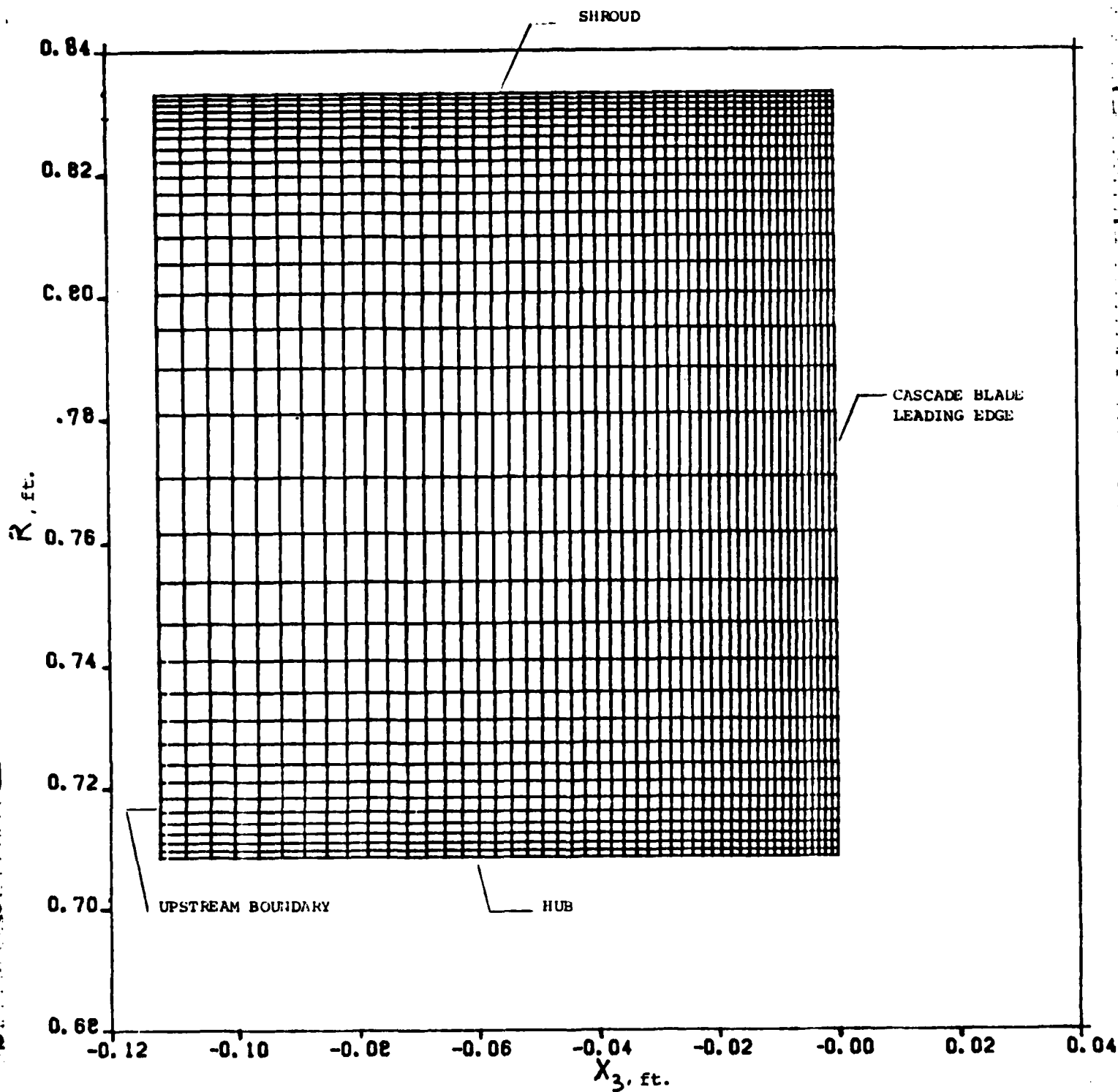
Figure 9. Finite difference mesh in a meridional plane passing through leading edge of cascade blade; mesh comprised of 35 horizontal lines and 50 vertical lines.
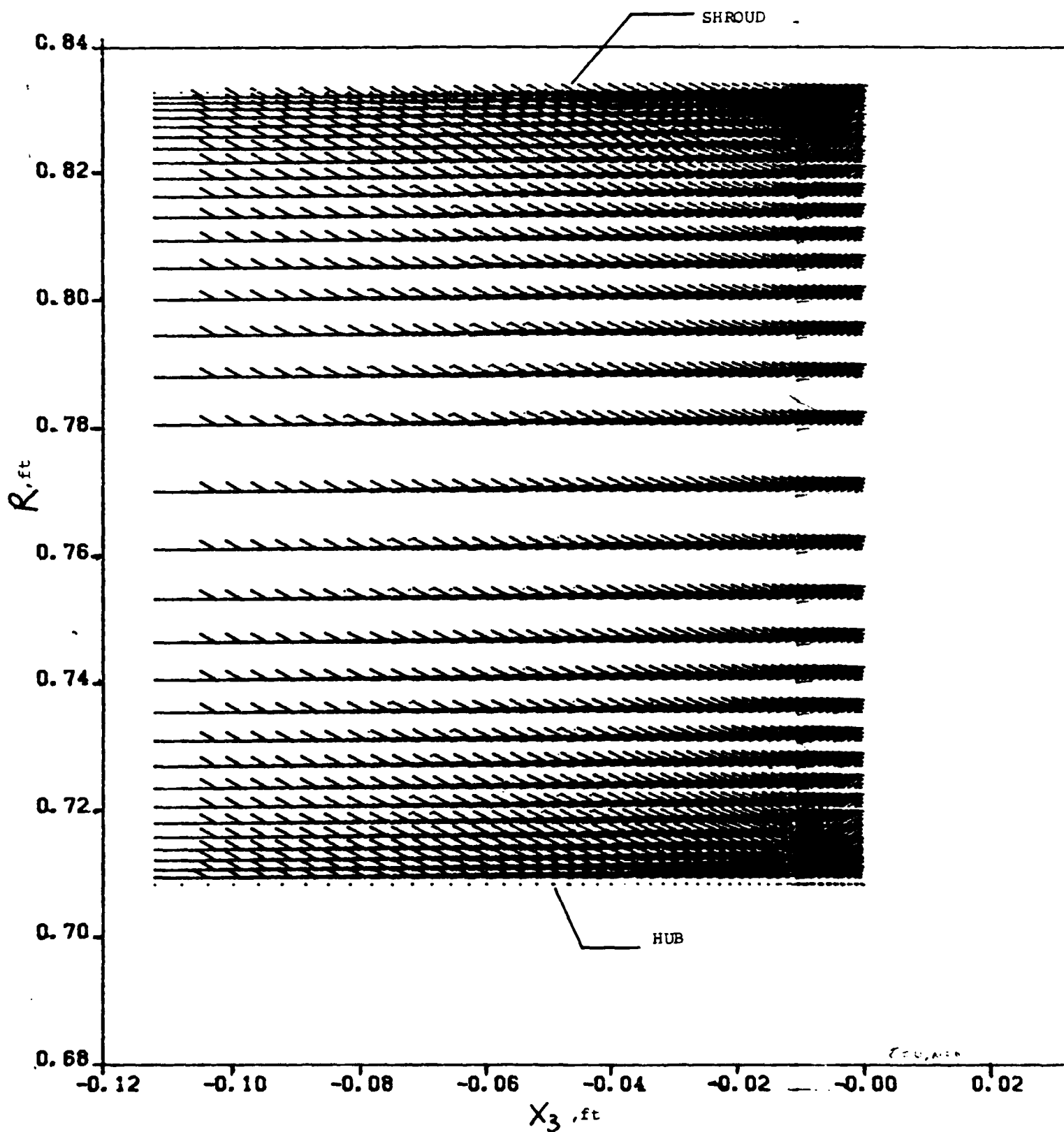
Figure 10: Velocity vector plot of the meridional flow field at $z = -.1745330$ radians, $t=0.0$
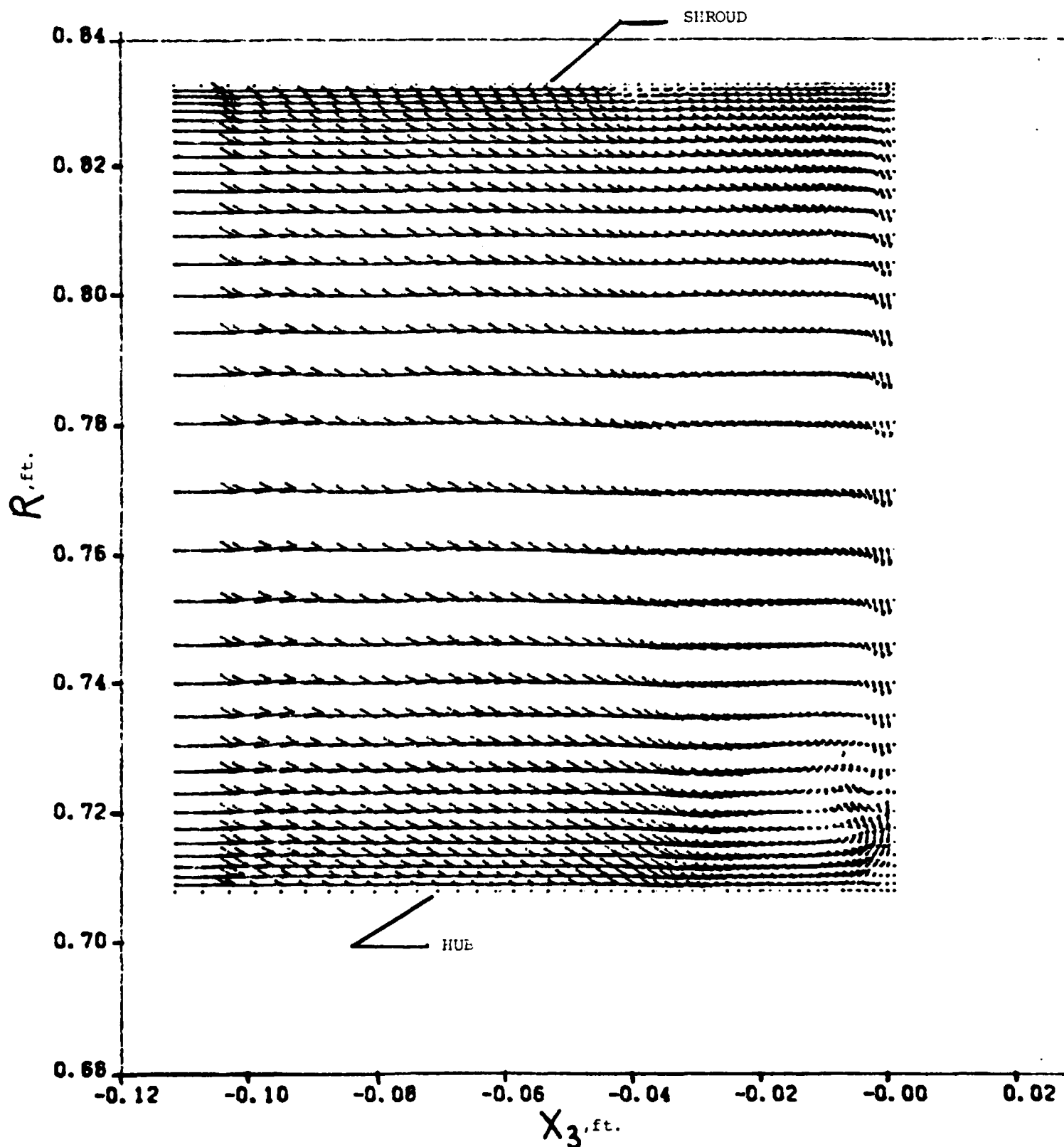
Figure 11. Velocity vector plot of the meridional flow field at z = -.1721619 radians
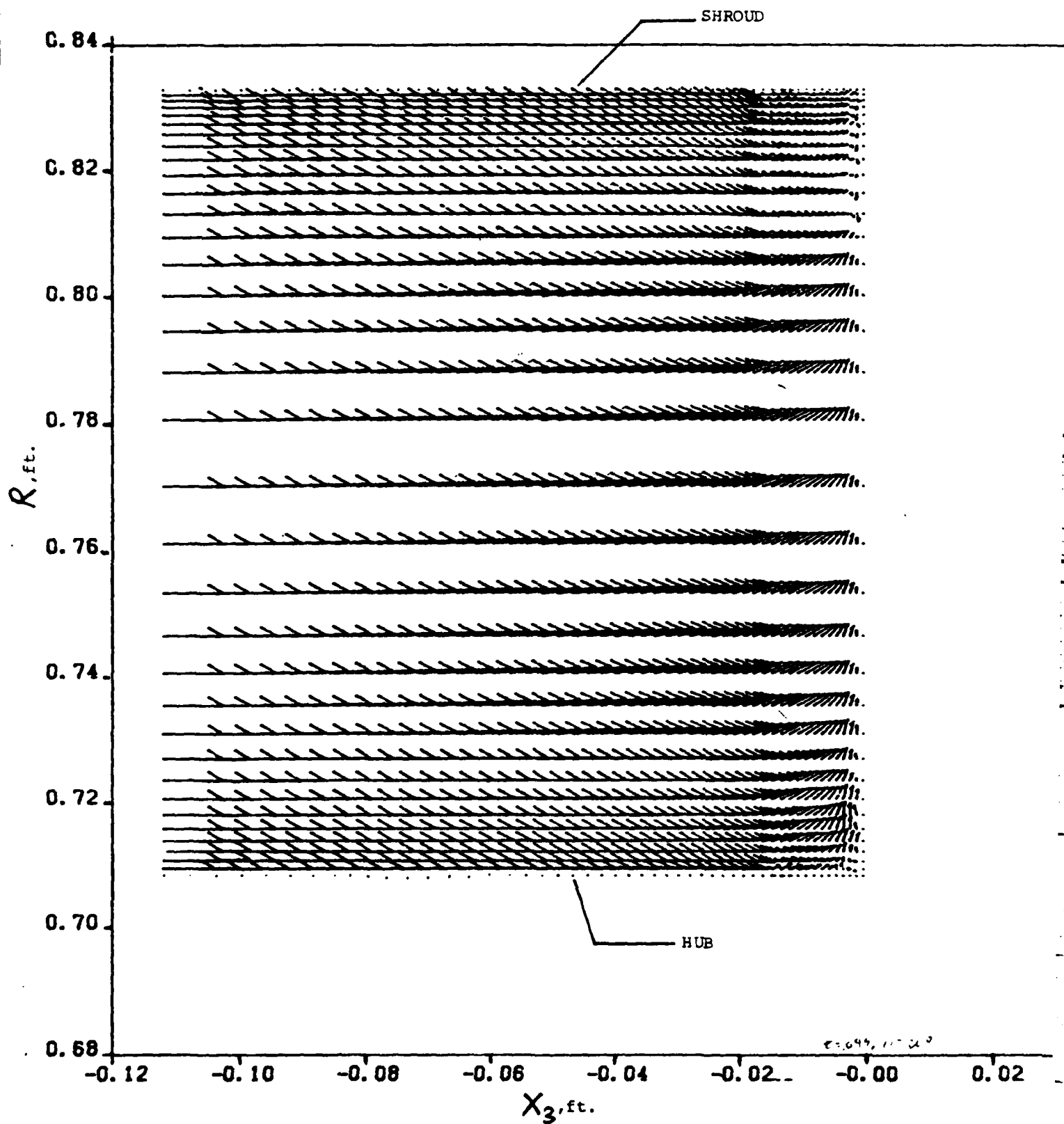
Figure 12. Velocity vector plot of the meridional flow field at z = -.1743968
radians, τ=.049
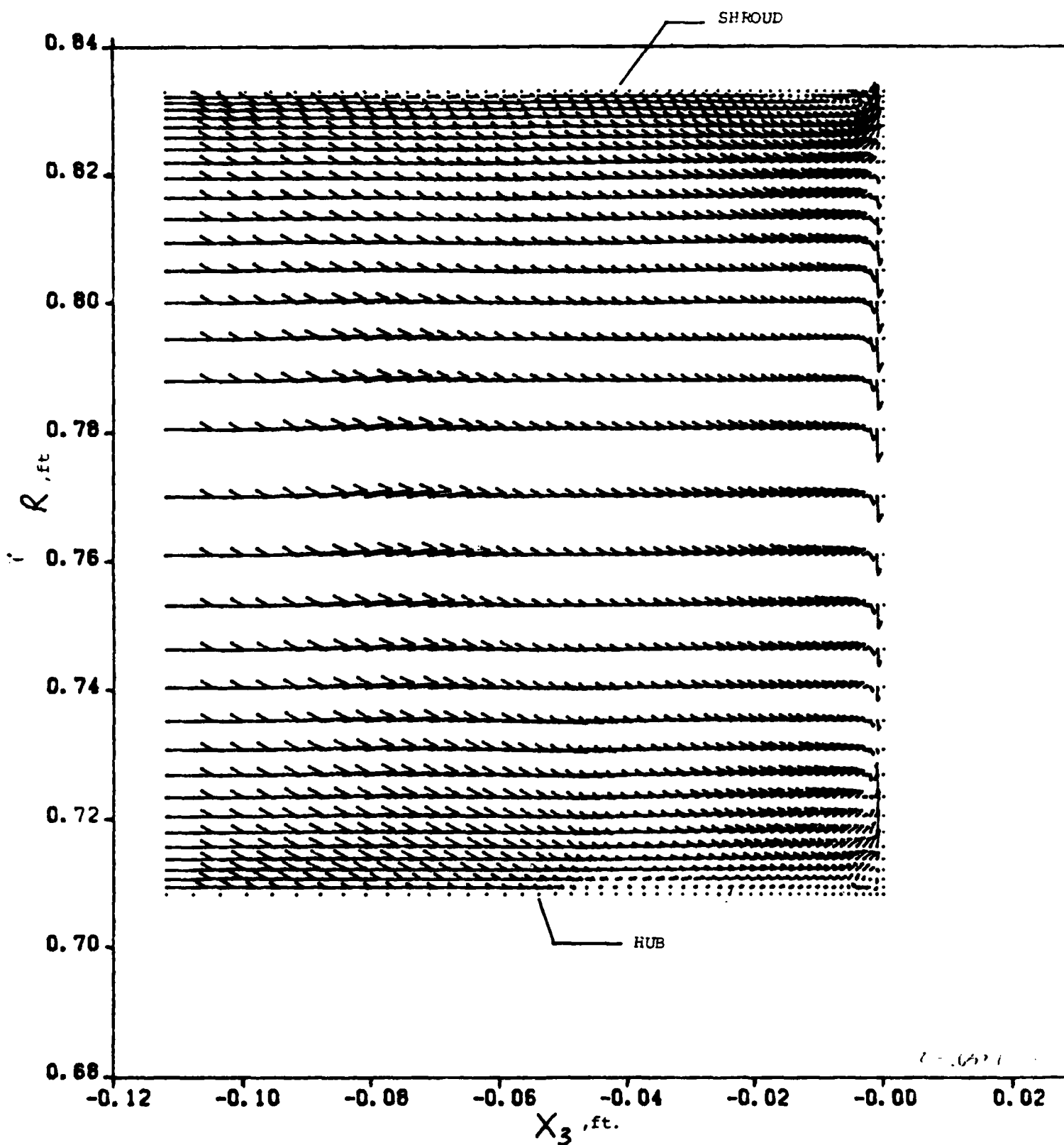
Figure 13. Velocity vector plot of the meridional flow field at z = -.17260446 radians, τ=.637
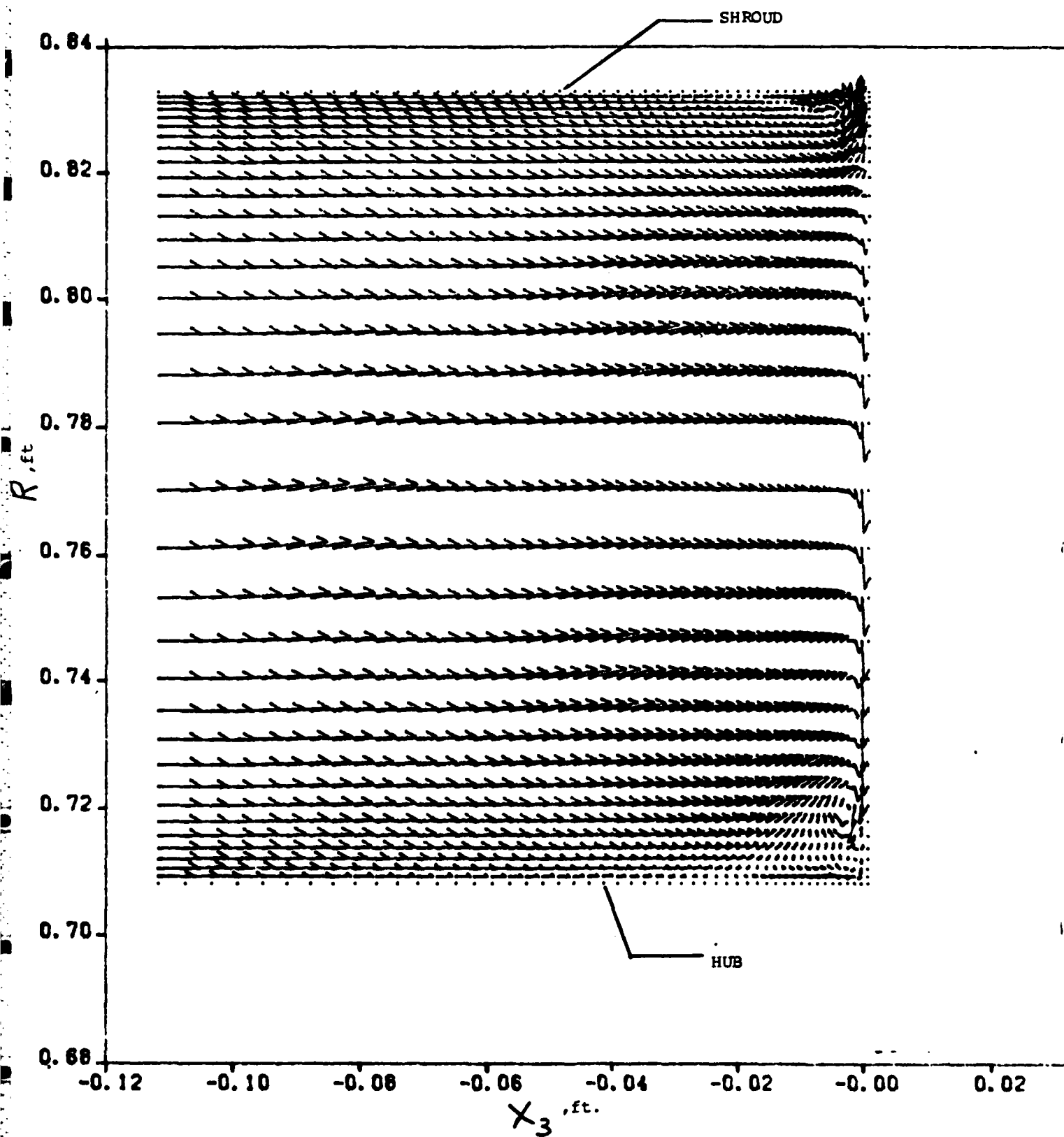
Figure 14. Velocity vector plot of the meridional flow field at z = -.1717460 radians;τ=1.01

47
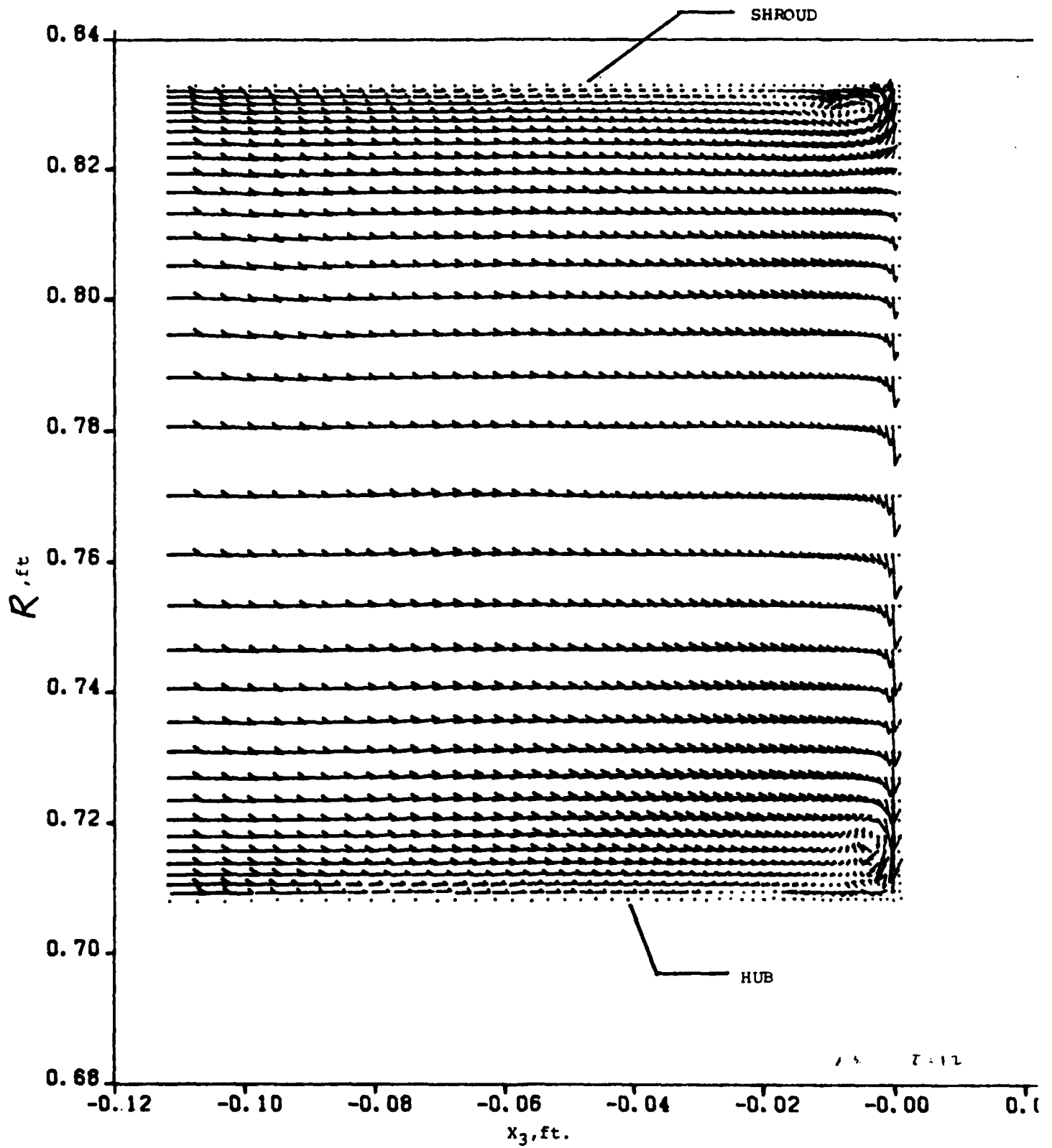
Figure 13.   Velocity vector plot of the meridional flow field at z = -.1712269
radians ;τ=1.20
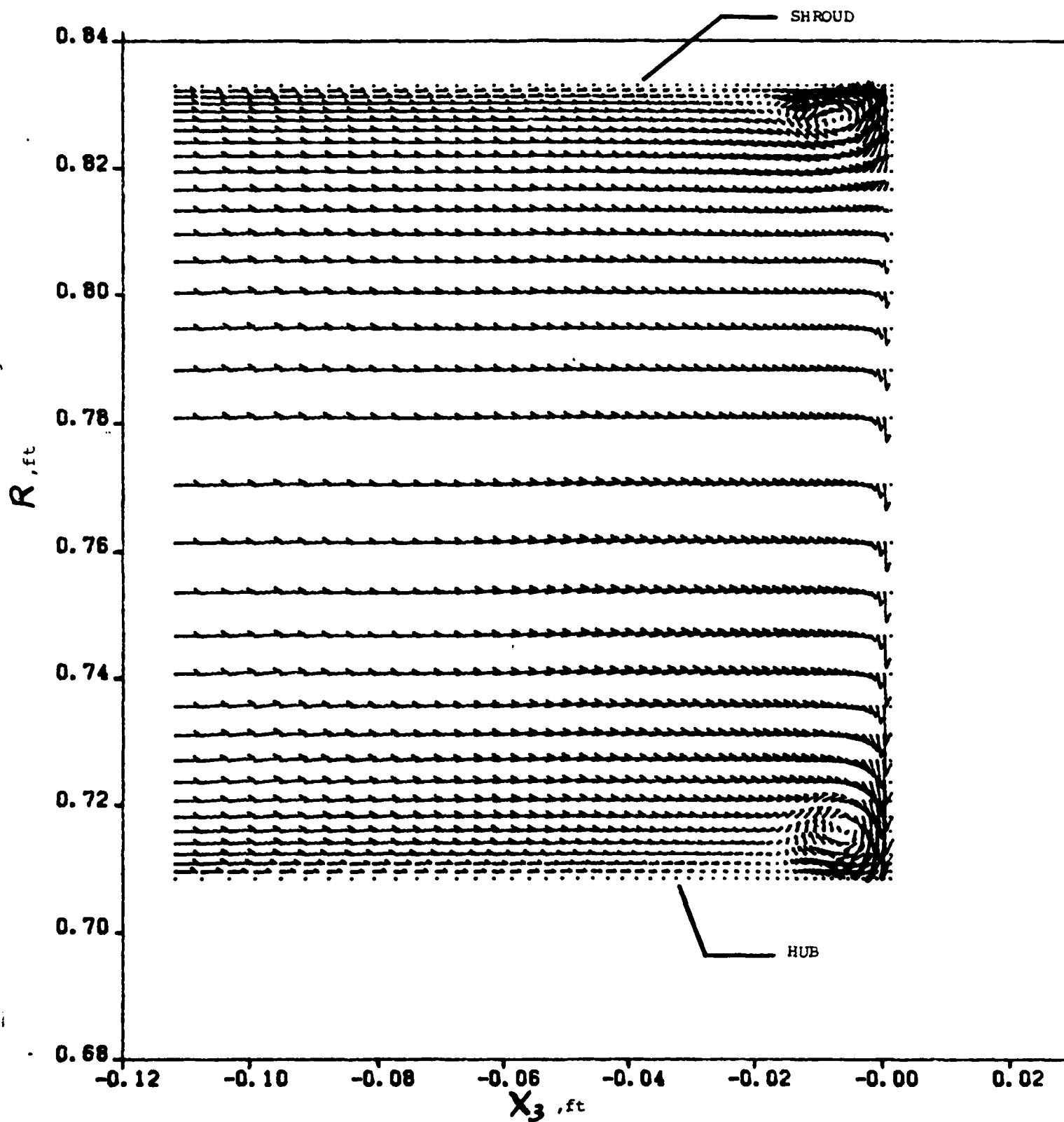
Figure 16.   Velocity vector plot of the meridional flow field at z = -.1692032
radians; τ=1.93
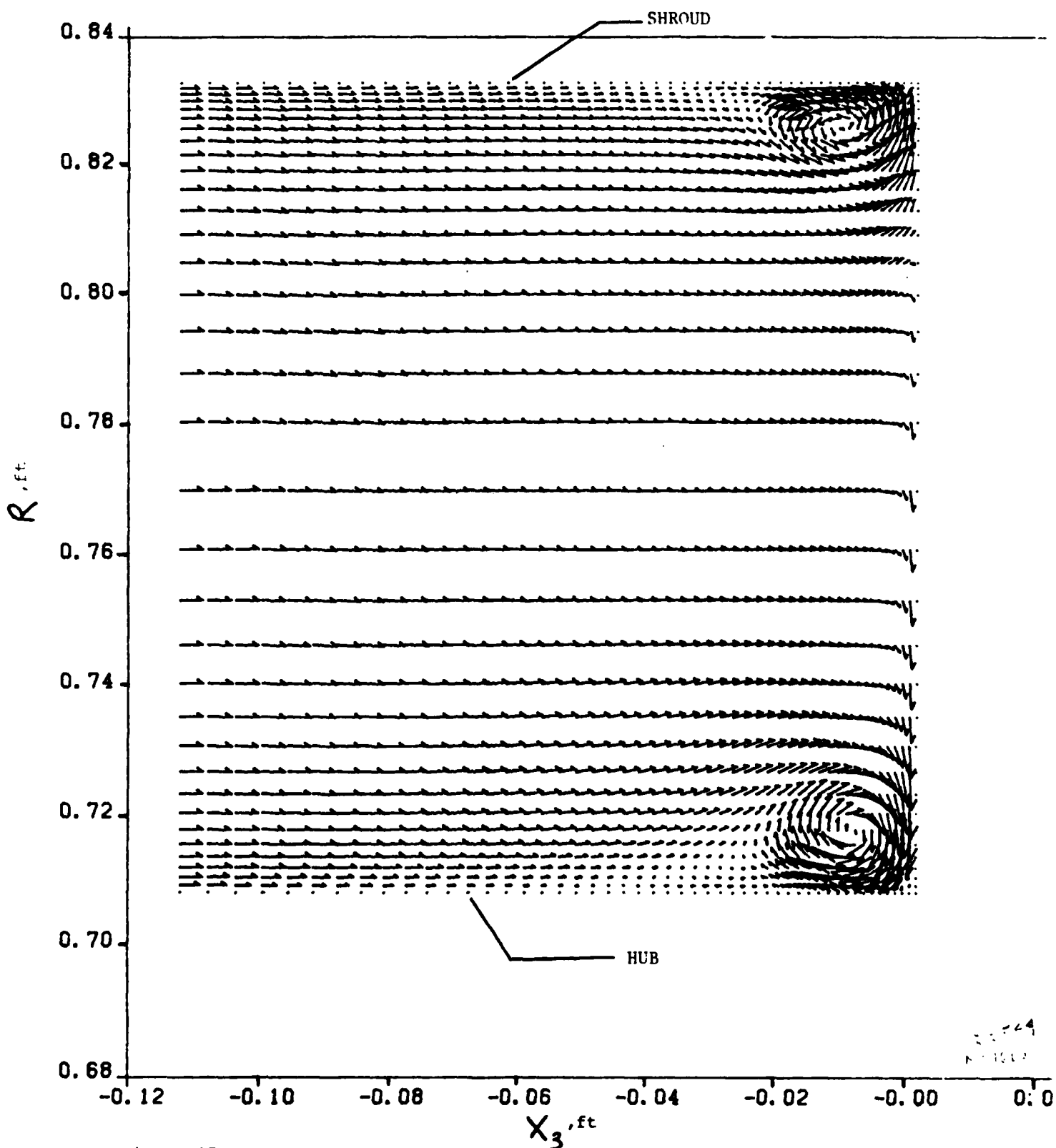
Figure 17.   Velocity vector plot of the meridional flow field at $Z = -.1660508$ radians; $t=5.44$
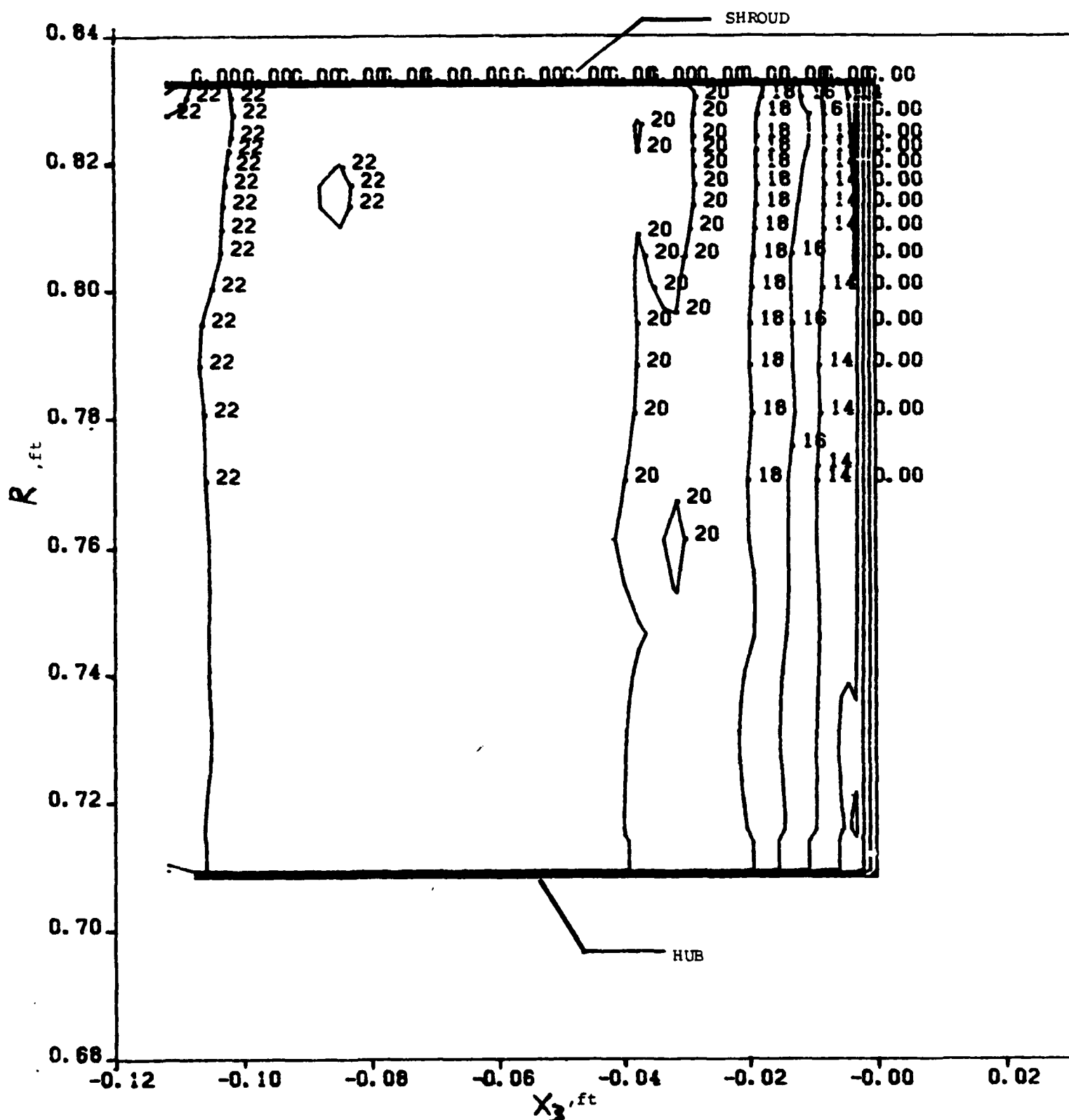
Figure 18. Critical velocity ratio contour plots at z = -.1745330 radians; ζ=0
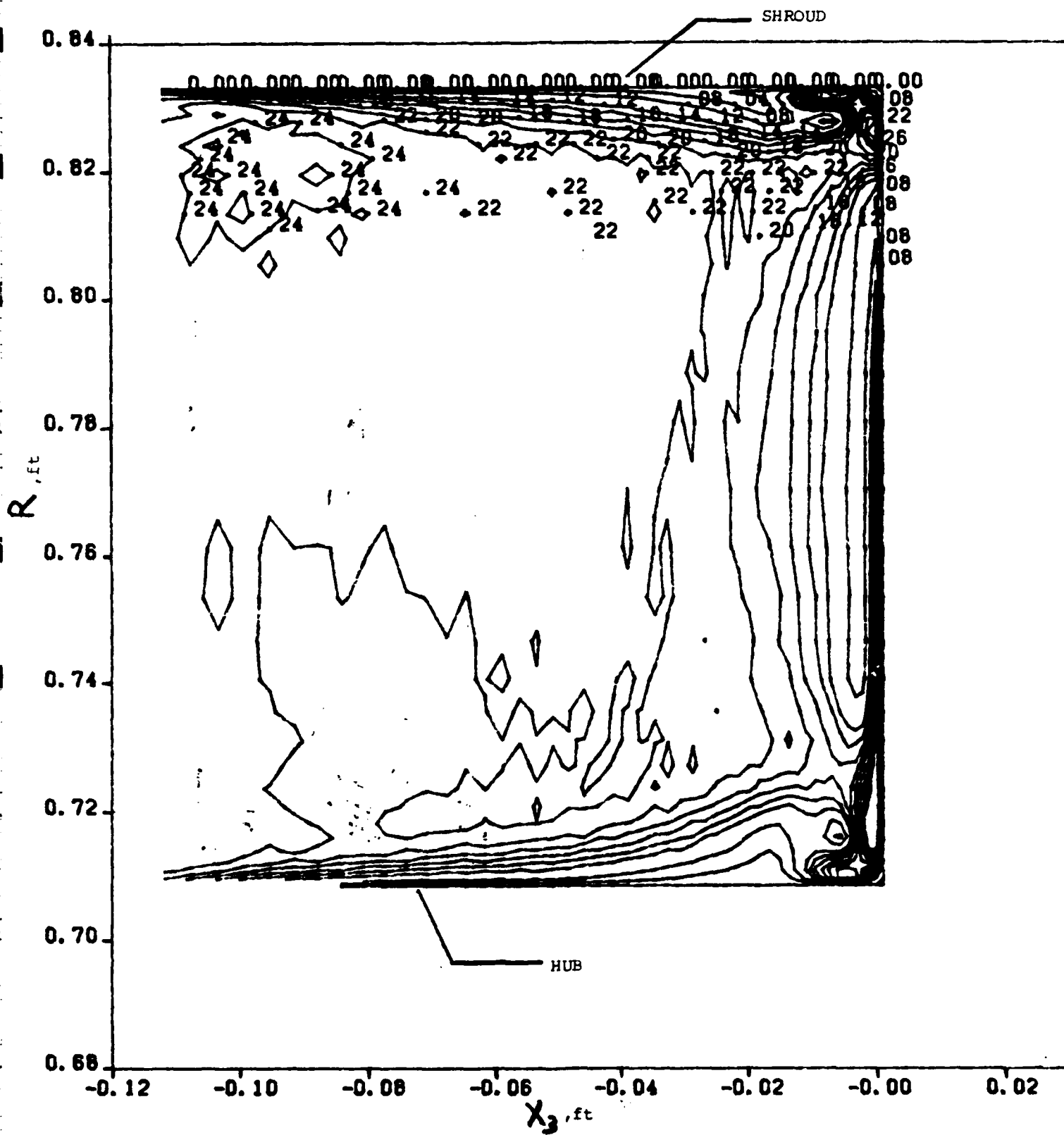
Figure 19.   Critical velocity ratio contour plots at z = -.1692032 radians;
             τ=1.93
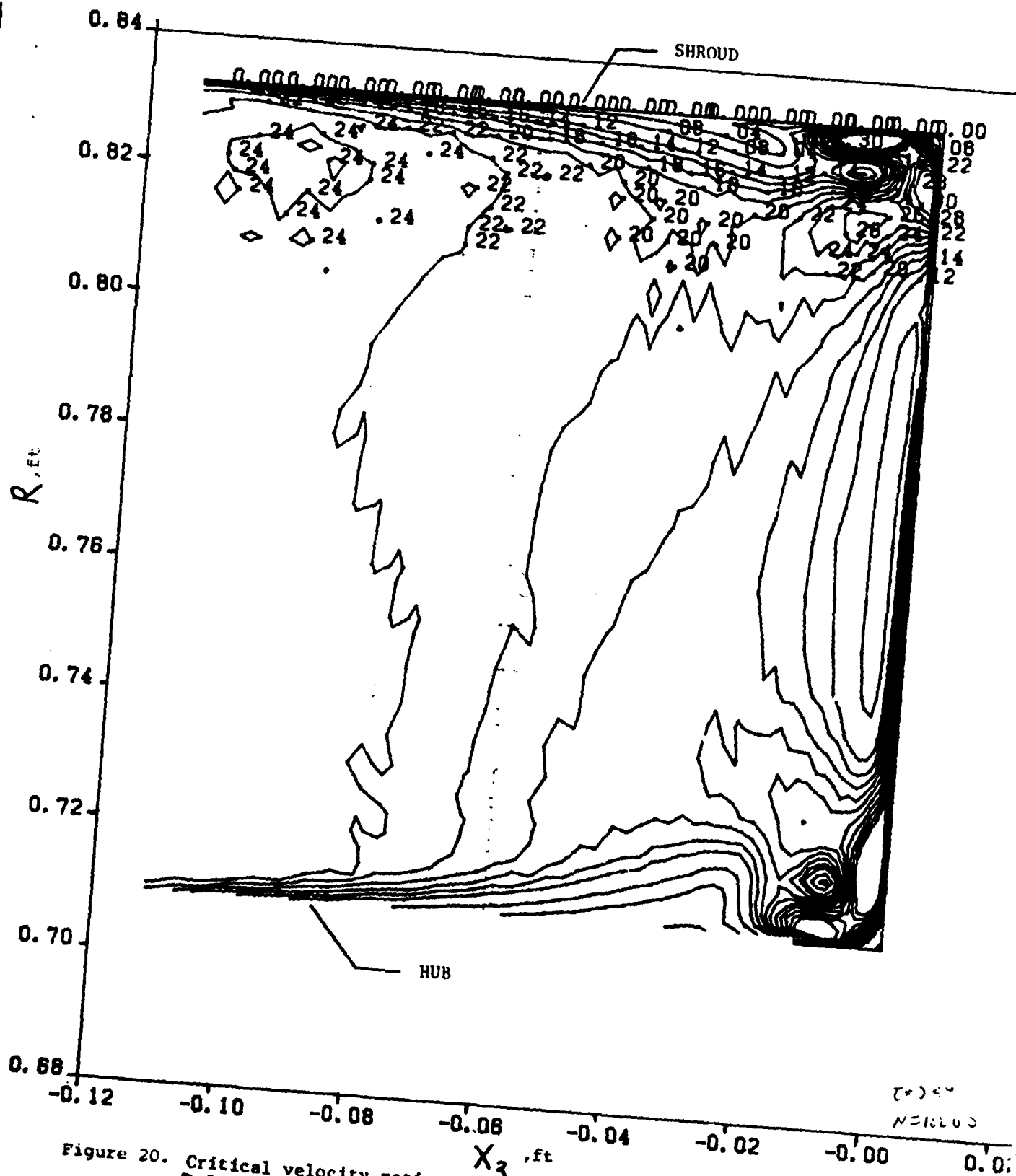
Figure 20. Critical velocity ratio contour plots at $\theta = -.1660580$ radians; t=5.44

Figure 21. Raster plot of the static pressures at points on the hub, mid-plane and shroud of the cascade
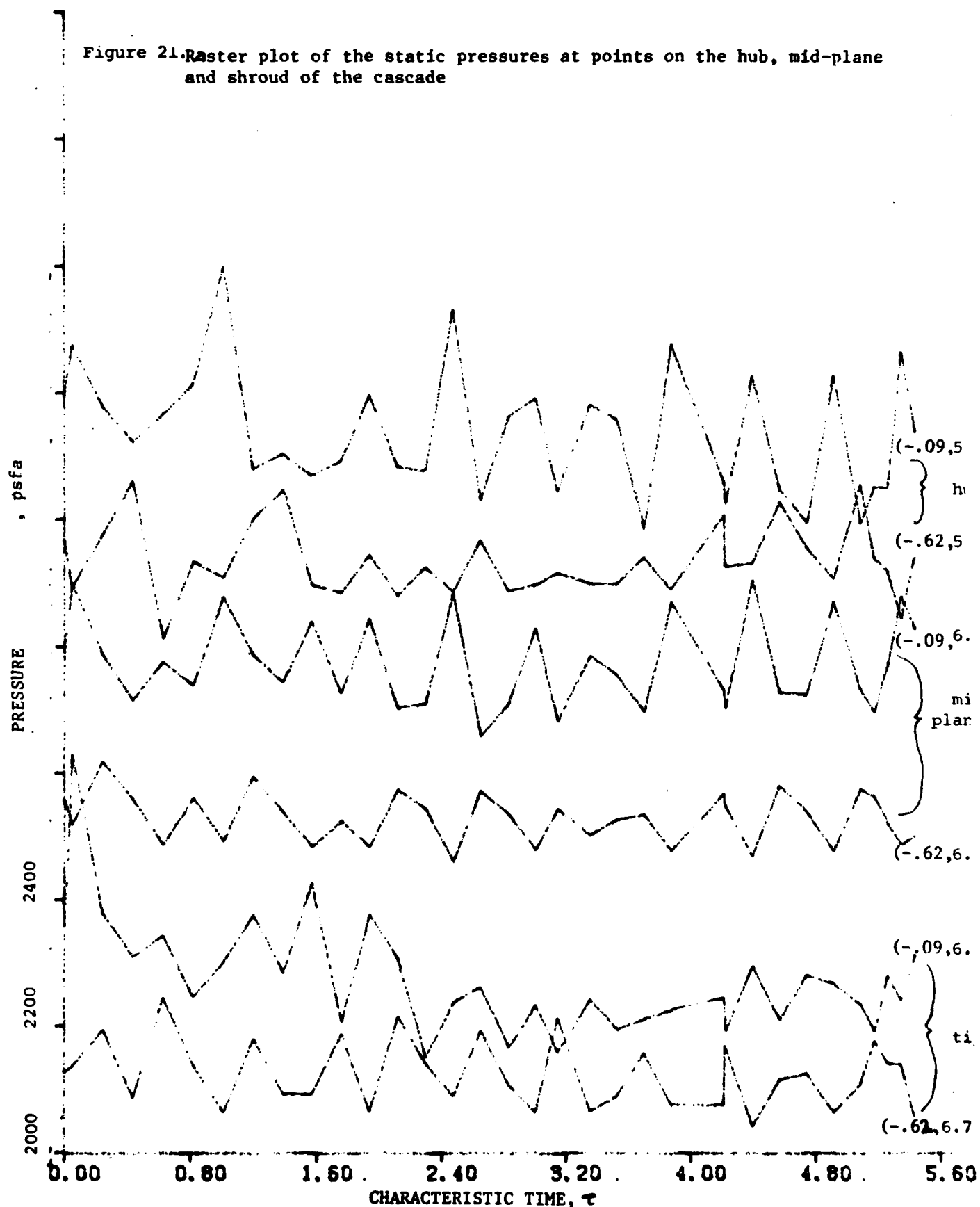
Figure 22. Raster plot of the mean static pressure at points on the hub,
          mid-plane and shroud of the cascade
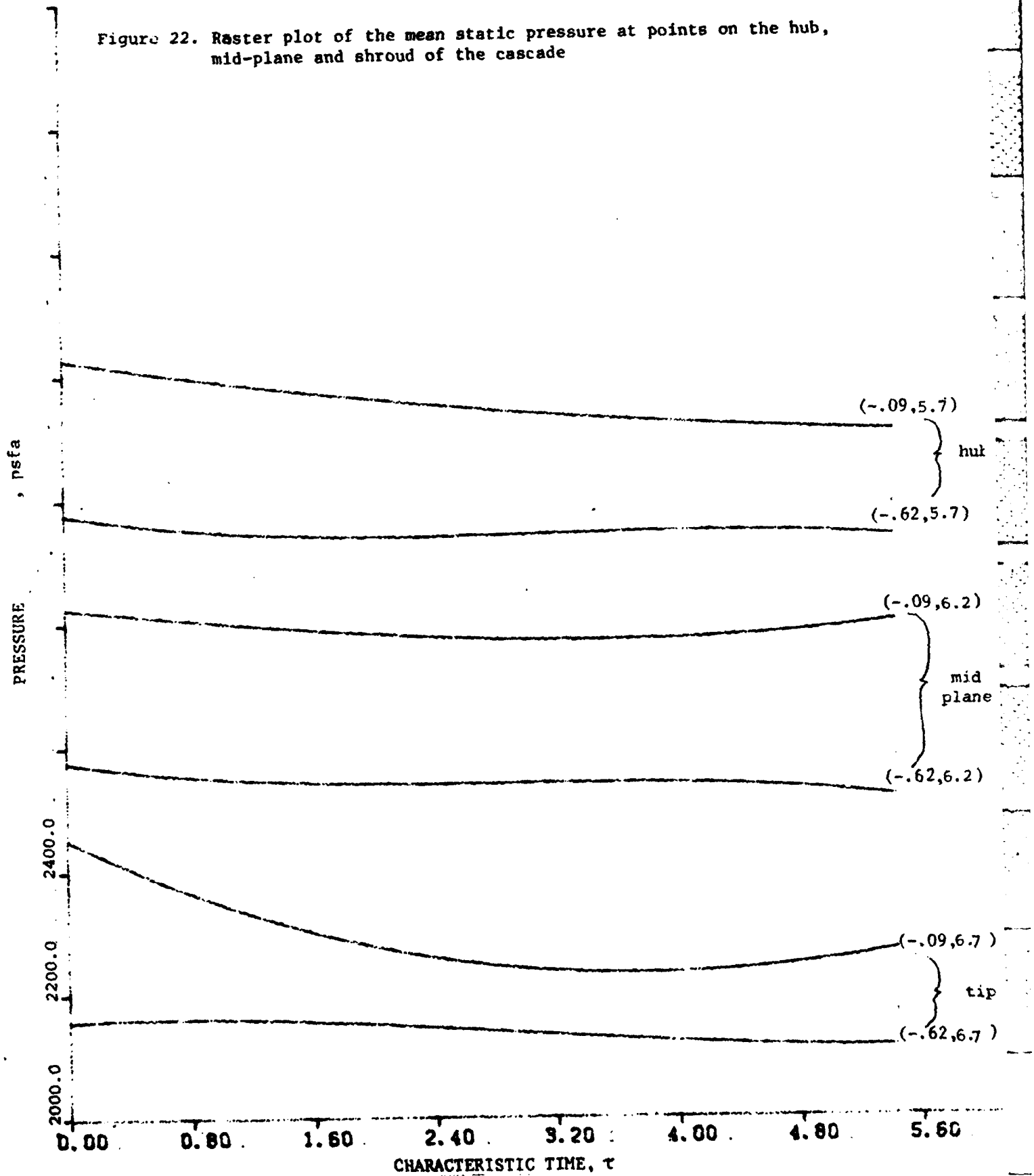
Figure 23. Raster plot of the static pressure fluctuation at points on the hub, mid-plane and shroud of the cascade.

56
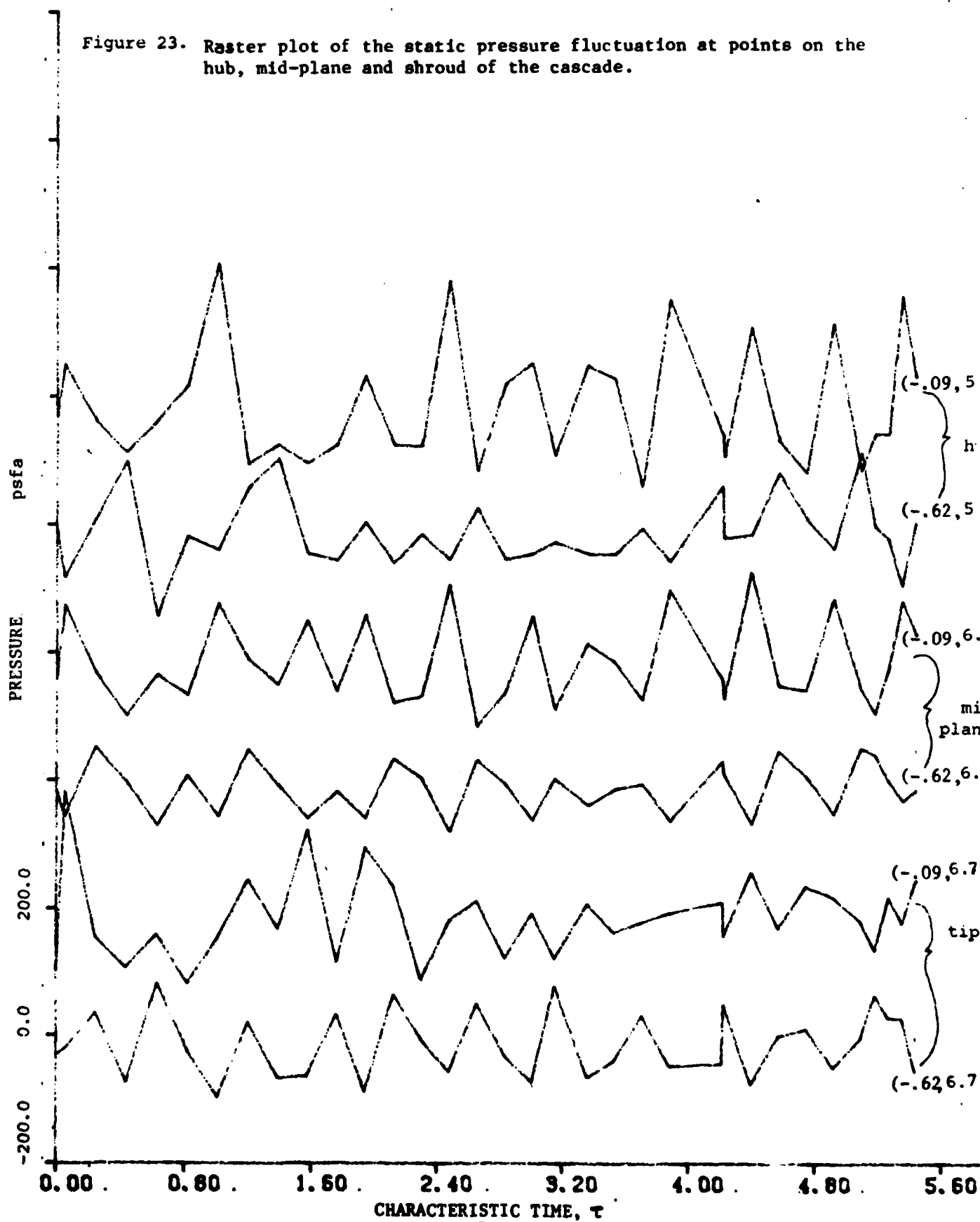
Figure 24. Power spectra of the pressure fluctation at points on the hub, mid-plane and shroud of the cascade
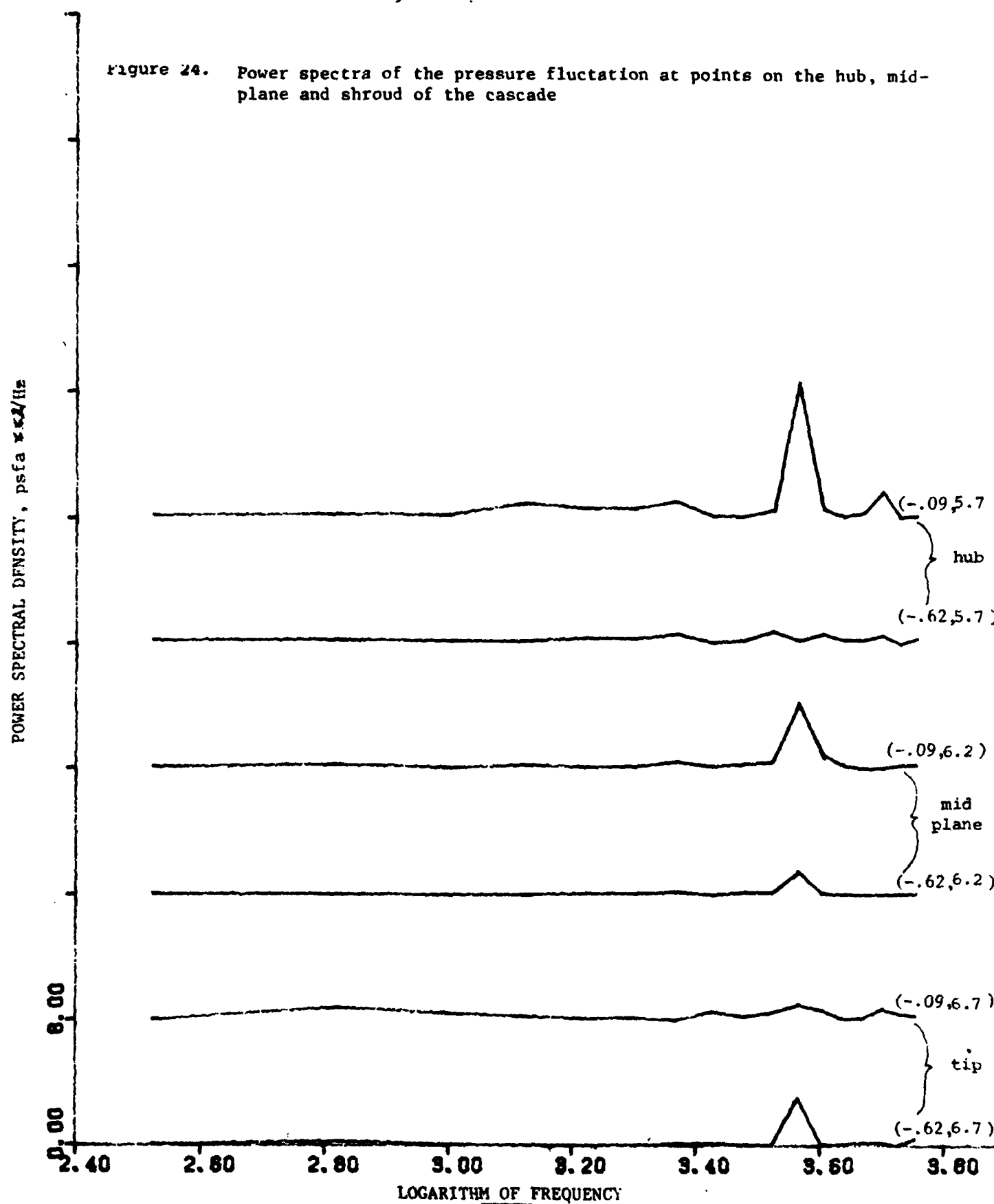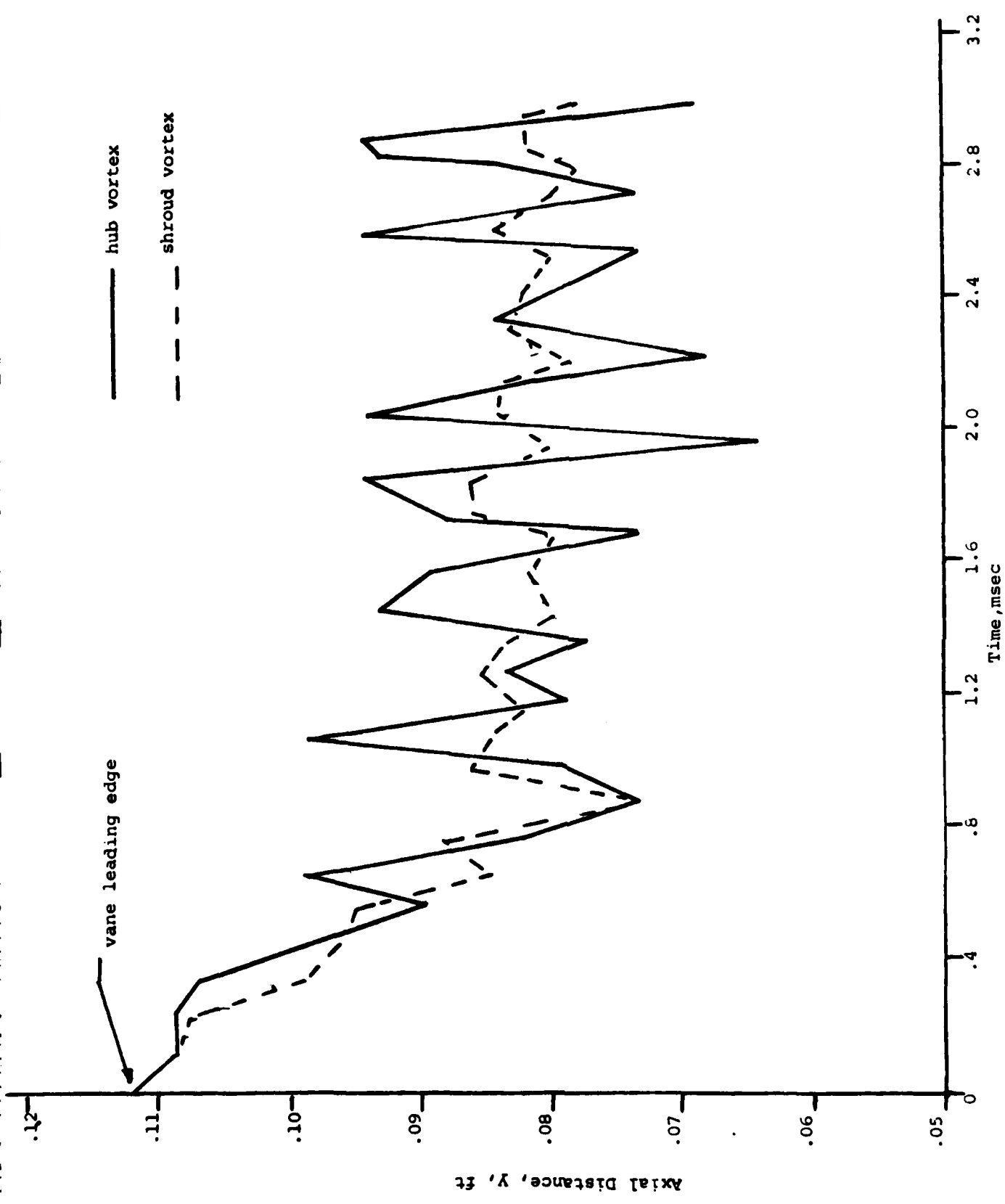
Figure 25. Variation of separation point locations for hub and shroud horseshoe vortex.

58
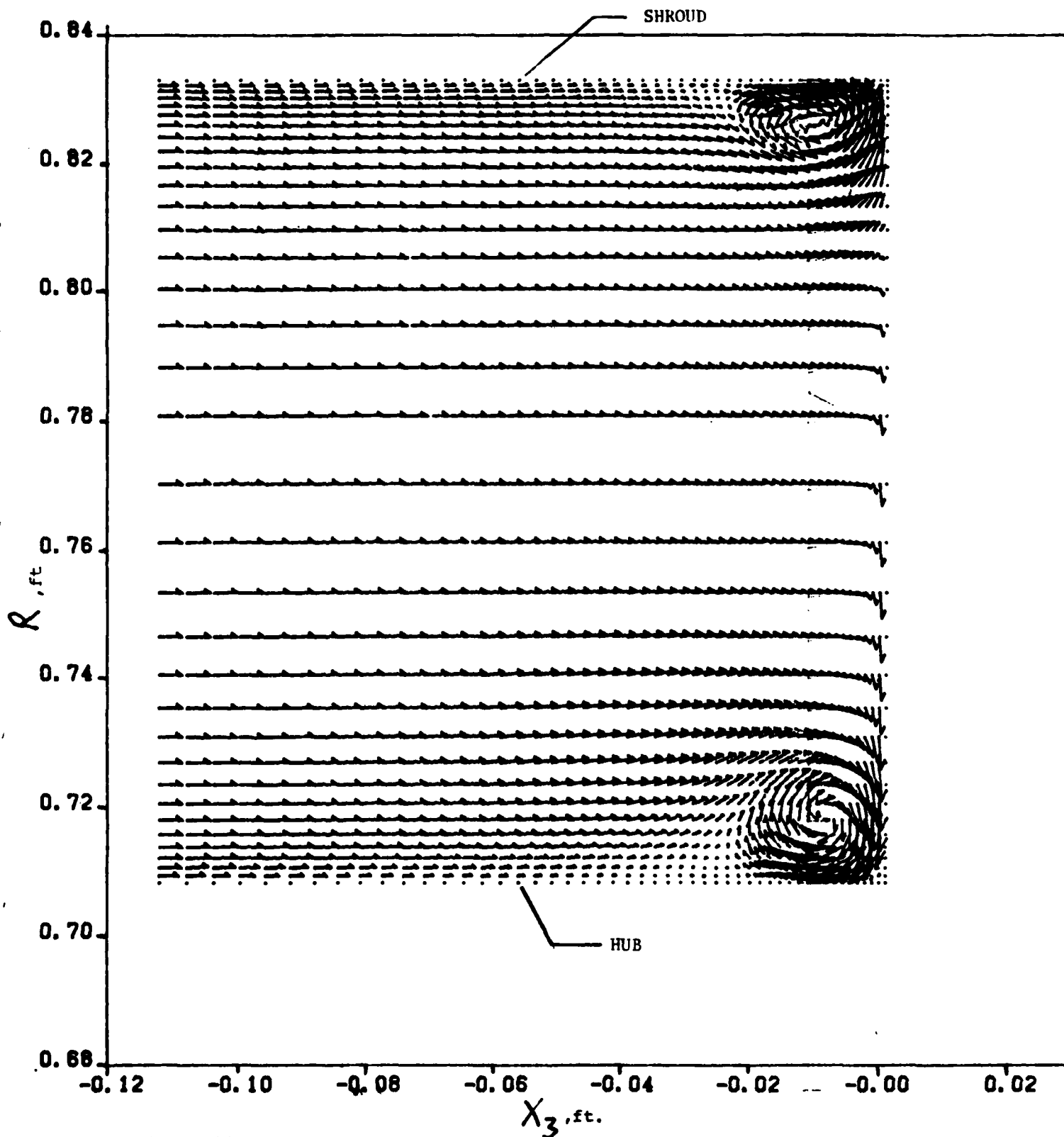
Figure 26. Velocity vector plot of the time-averaged meridional flow field at
$\theta = -.1660508$ radians; _____
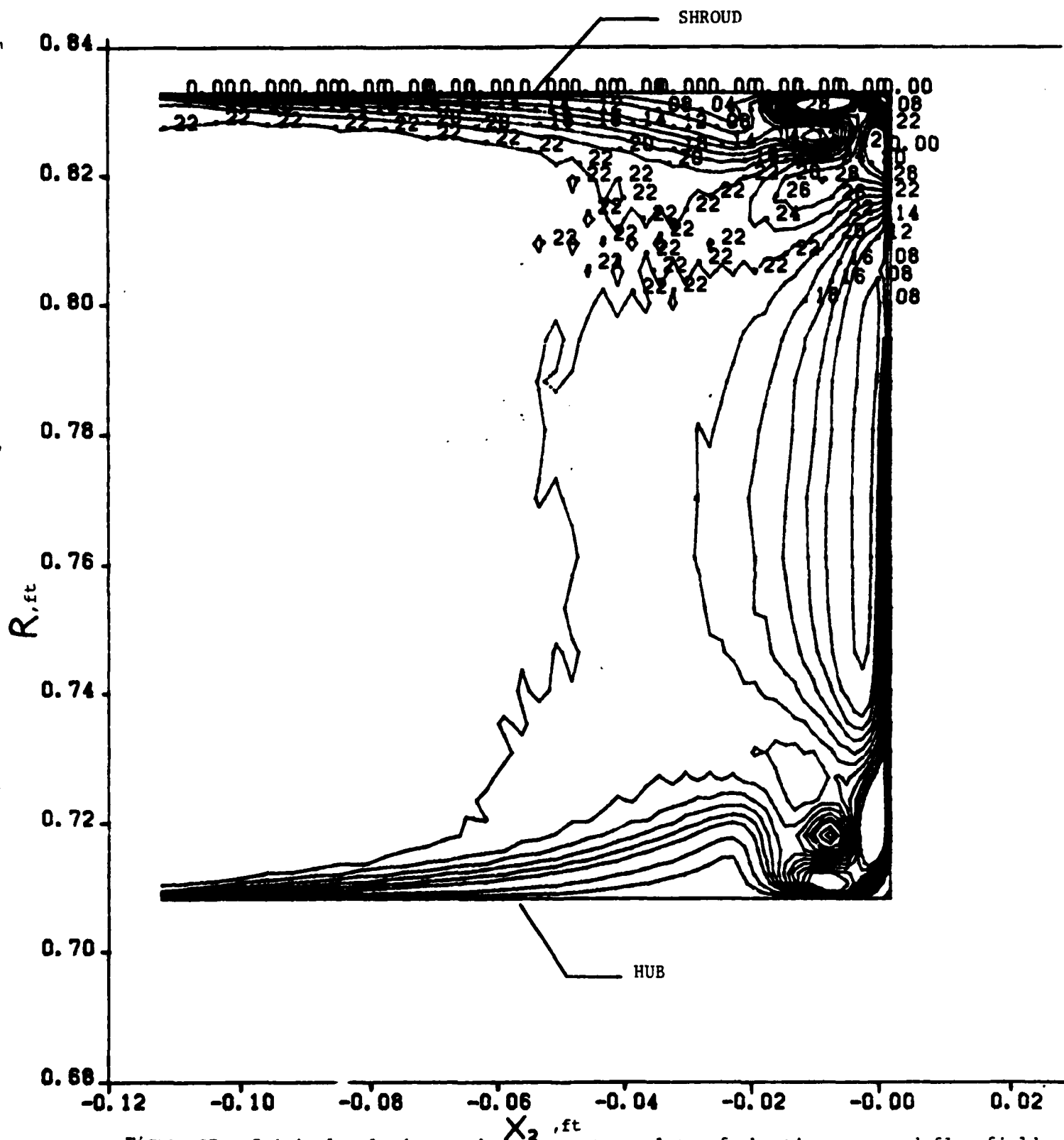
Figure 27. Critical velocity ratio X_3 ,ft contour plots of the time-averaged flow field at ө =-.1660508 radians
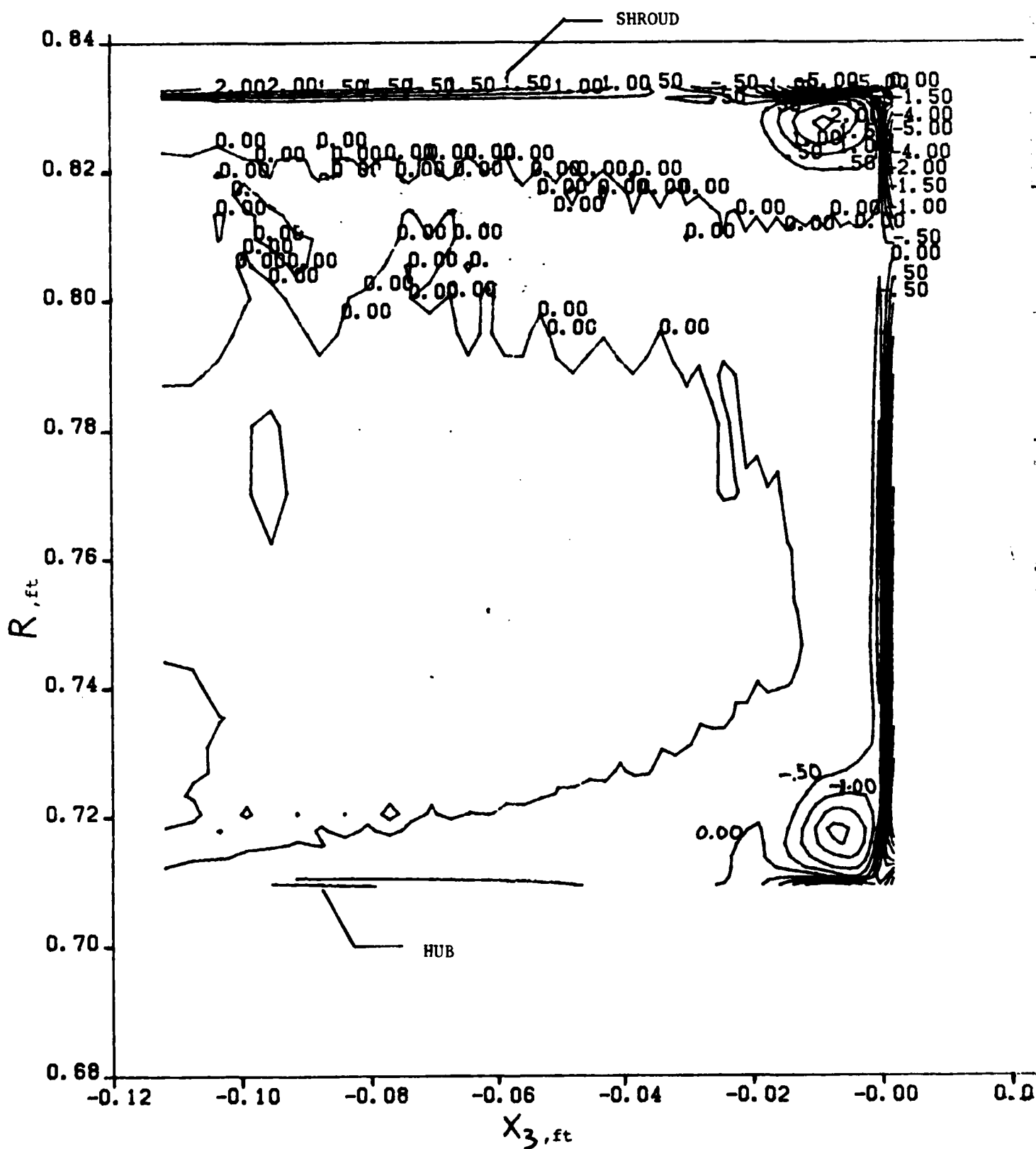
Figure 28. Vorticity ratio contour plots of the time-averaged flow field at $\theta = -.1660508$ radians
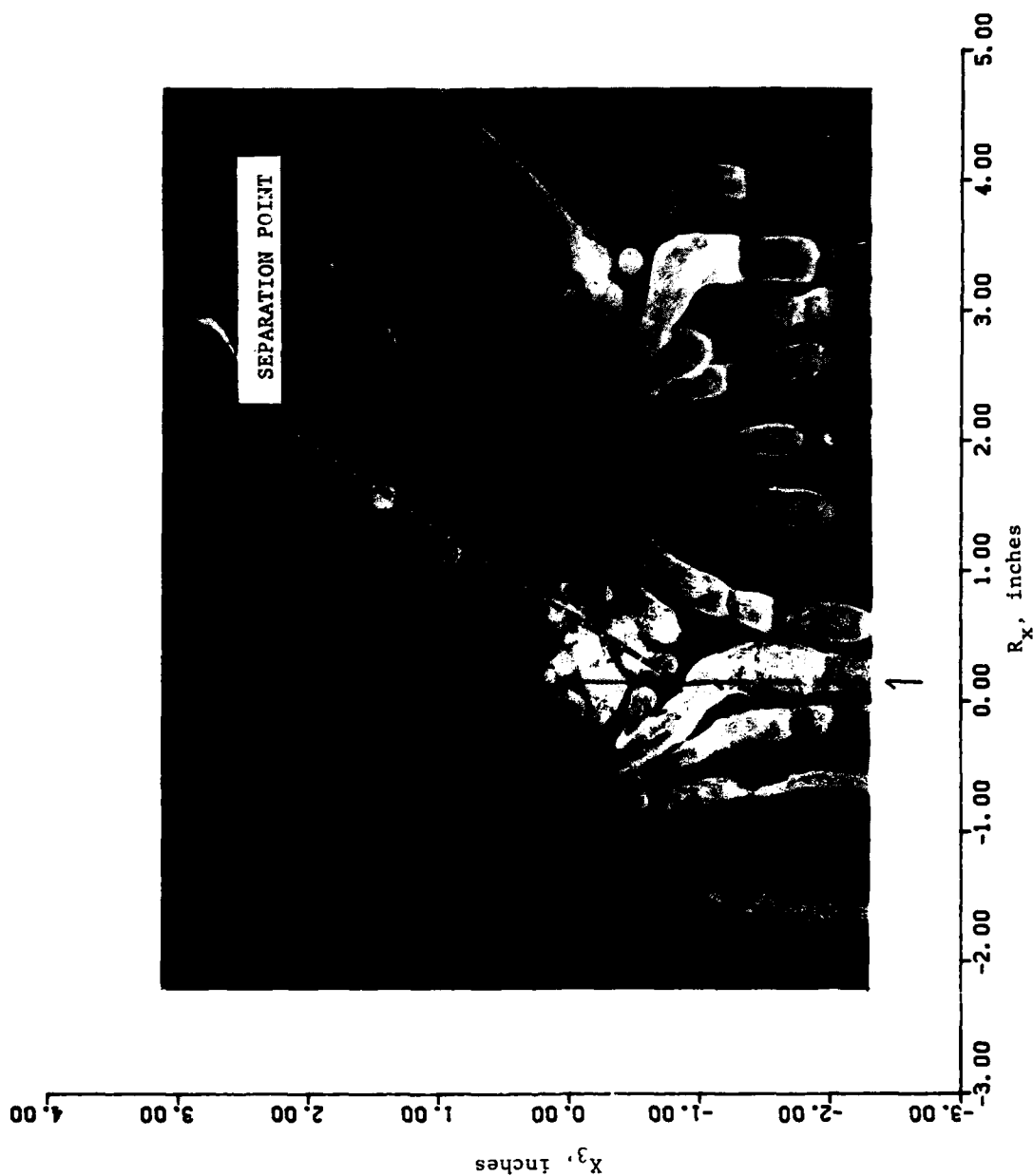
Figure 29. Comparison of calculated normalized velocity vectors along the hub with a photograph of hub endwall oil traces; vectors in separation region not shown.

62
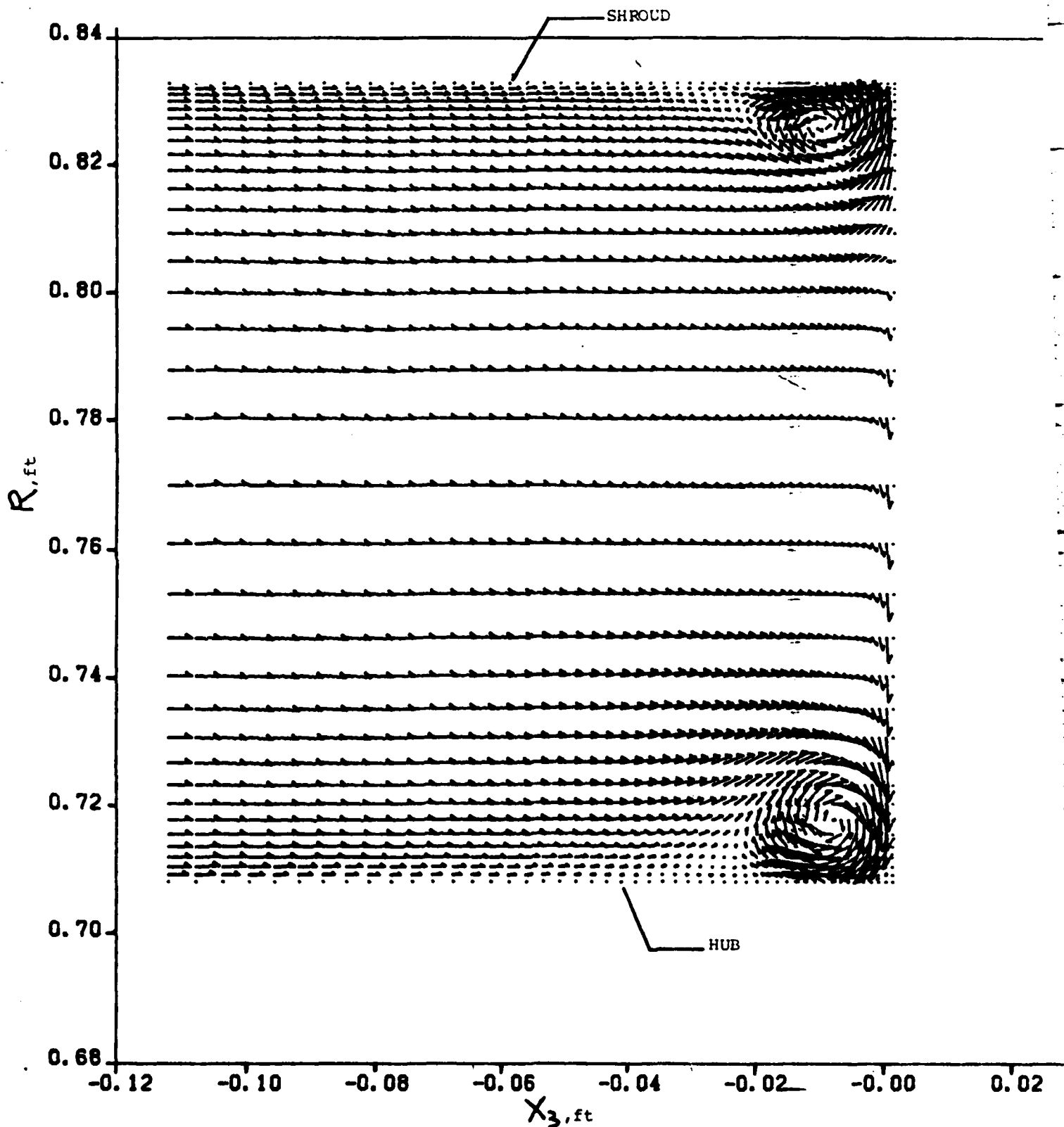
Figure 30. Velocity vector plot of the turbulent meridional flow field at z = -.1661652 radians; time after start of computation 2.42 ms.
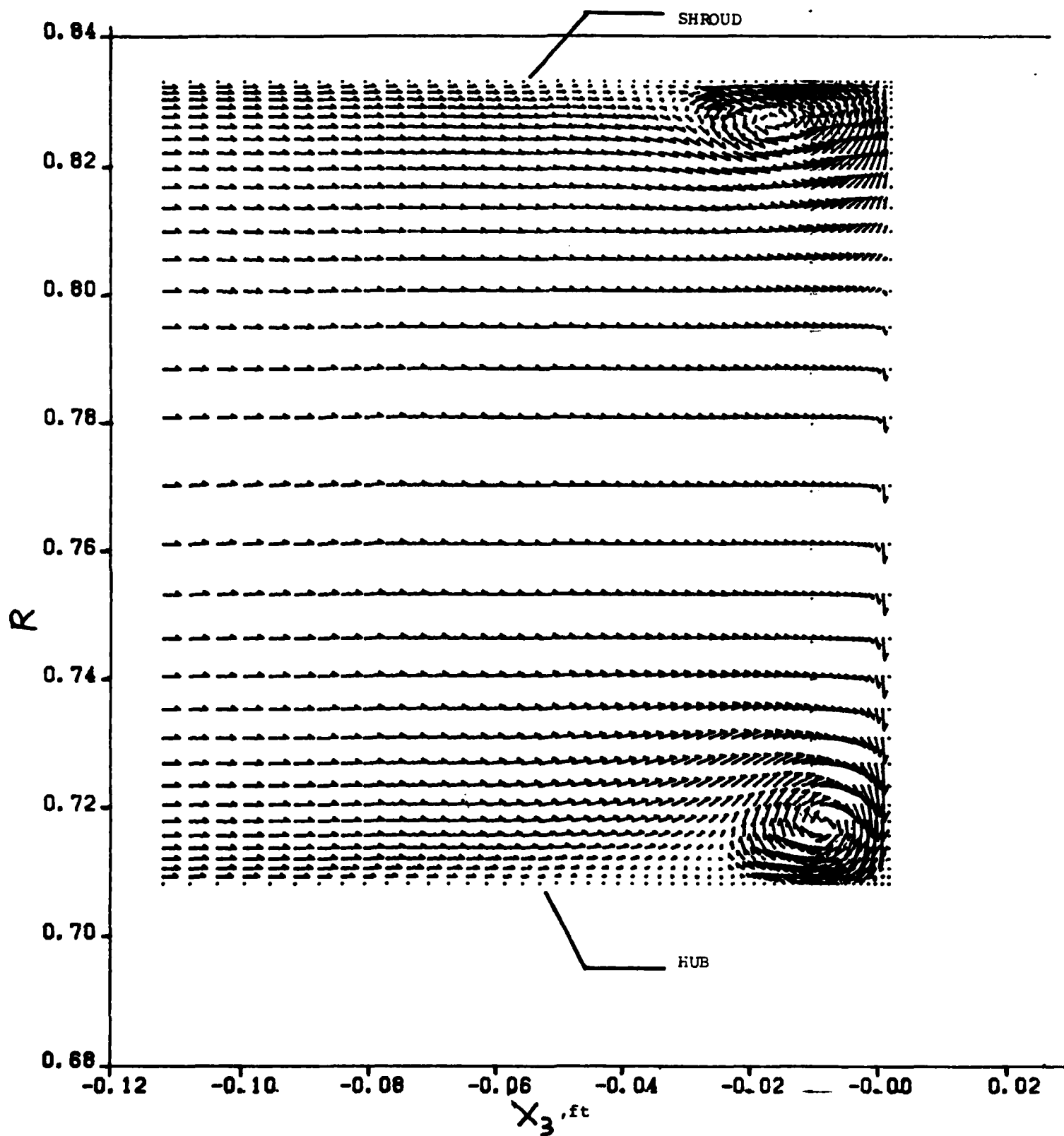
Figure 31. Velocity vector plot of the laminar meridional flow field at z = -.1661270 radians; τ=.346
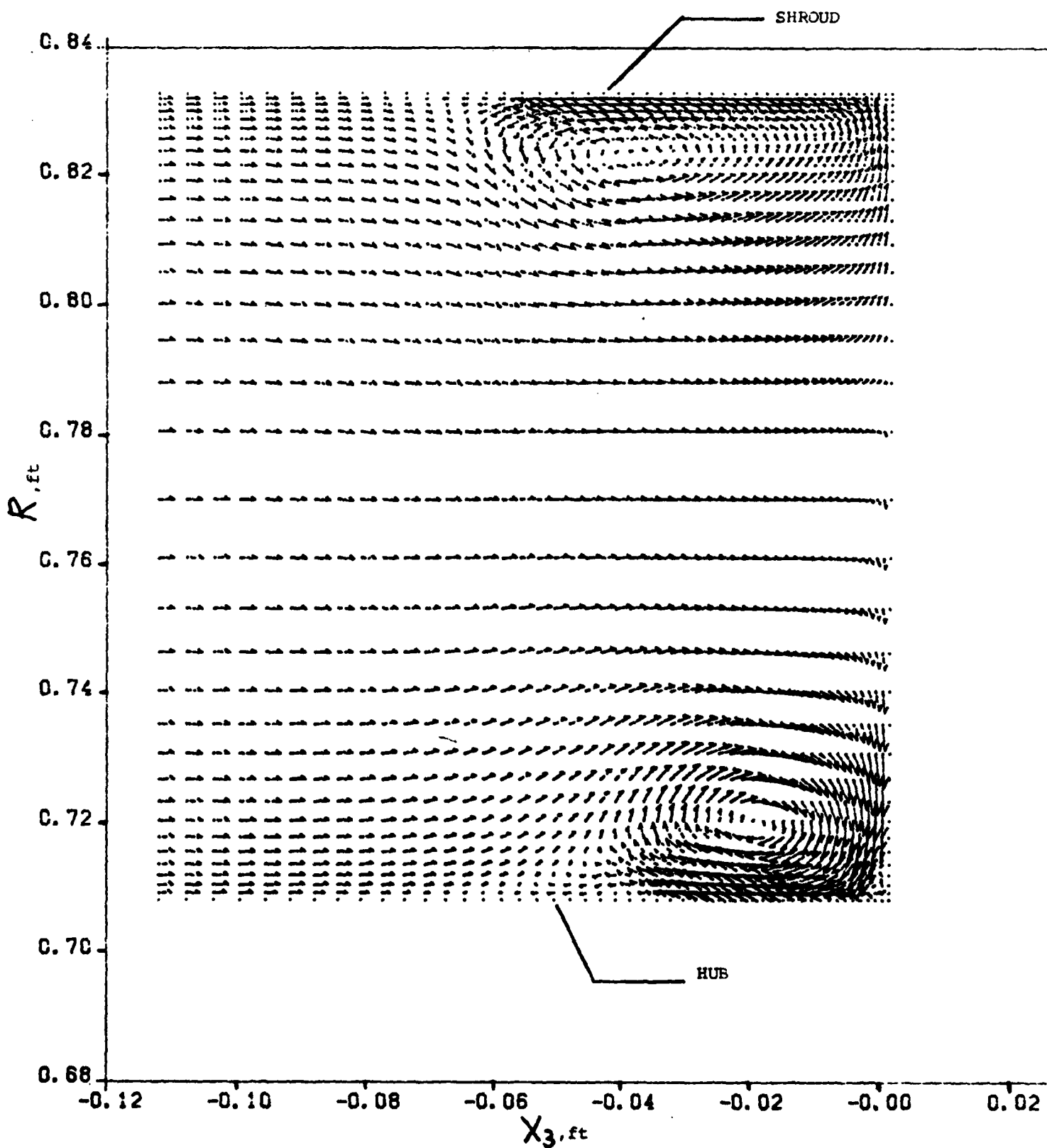
Figure 32. Velocity vector plot of the laminar meridional flow field at z = -.165993(
radians;t=1.55
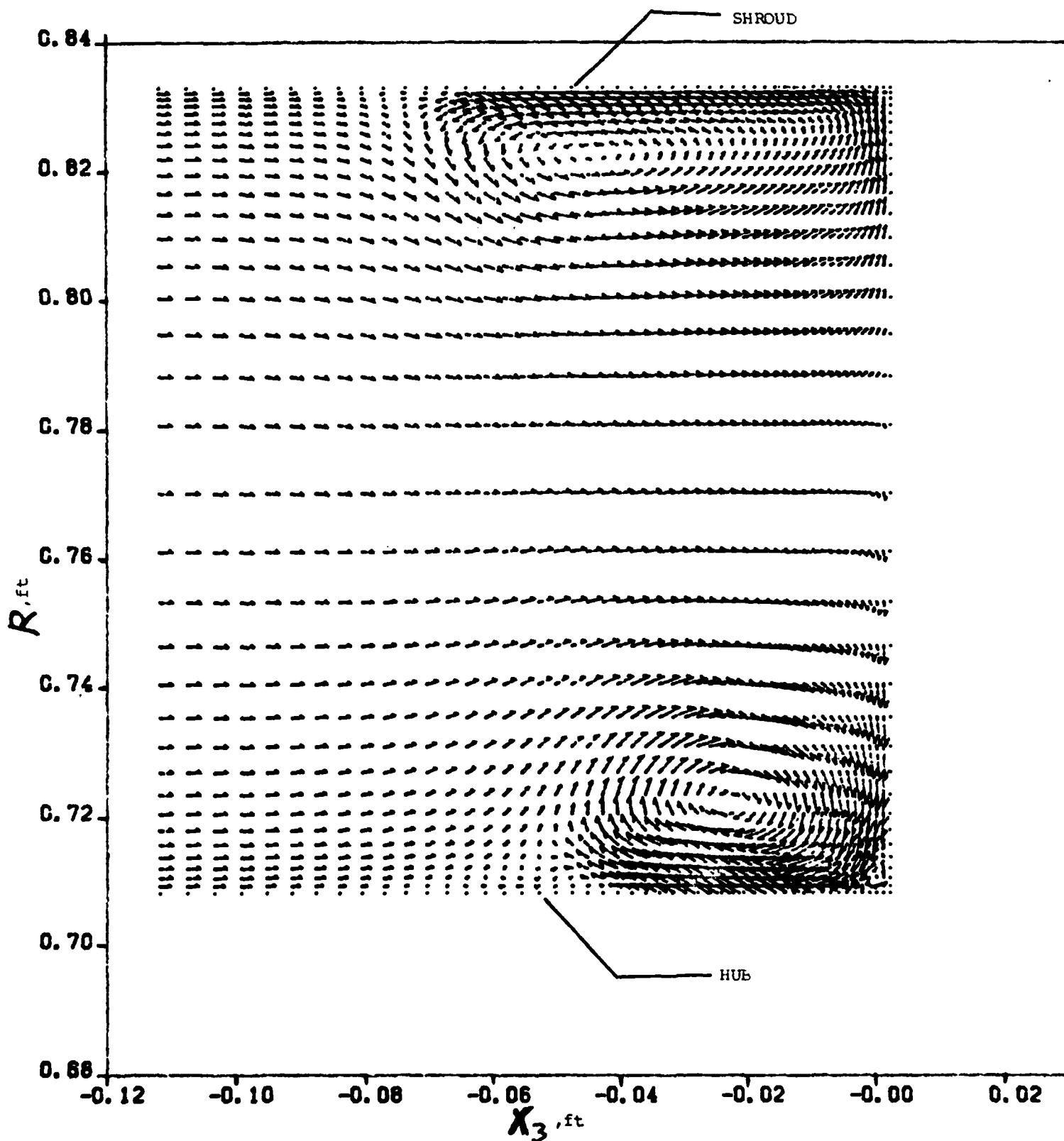
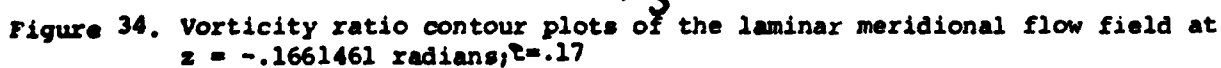Figure 33. Velocity vector plot of the laminar meridional flow field at z = -.1659364
radians; τ=2.09

Figure 34. Vorticity ratio contour plots of the laminar meridional flow field at
z = -.1661461 radians; t=.17

Figure 35. Vorticity ratio contour plots of the laminar meridional flow field at z = -.1659364 radians; t=2.09

Figure 36.   Raster plot of the static pressures at points on the hub, mid-plane and shroud of the cascade; laminar flow calculation.
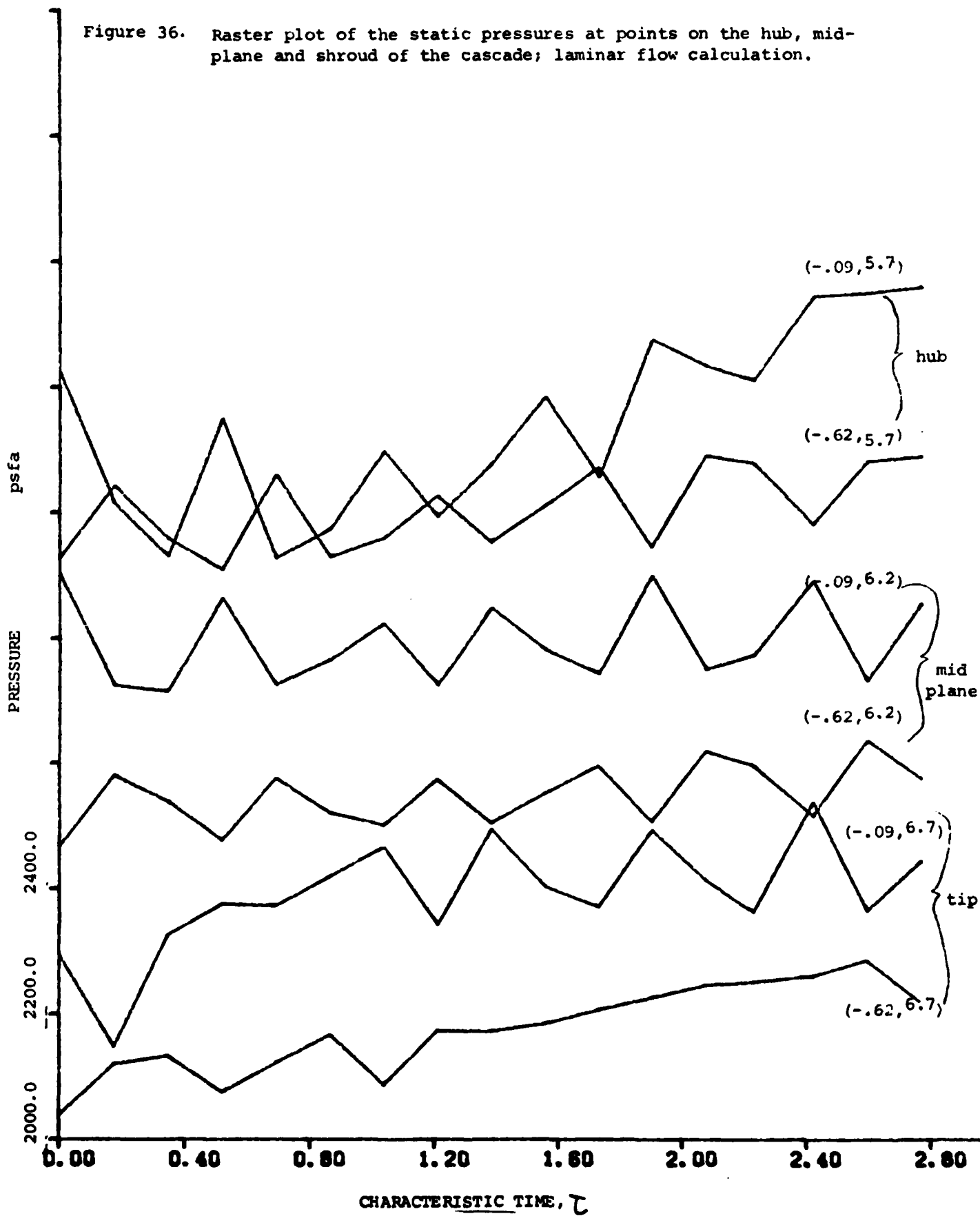
69

Figure 37. Raster plot of the mean static pressure at points on the hub, mid-plane and shroud of the cascade; laminar flow calculation.
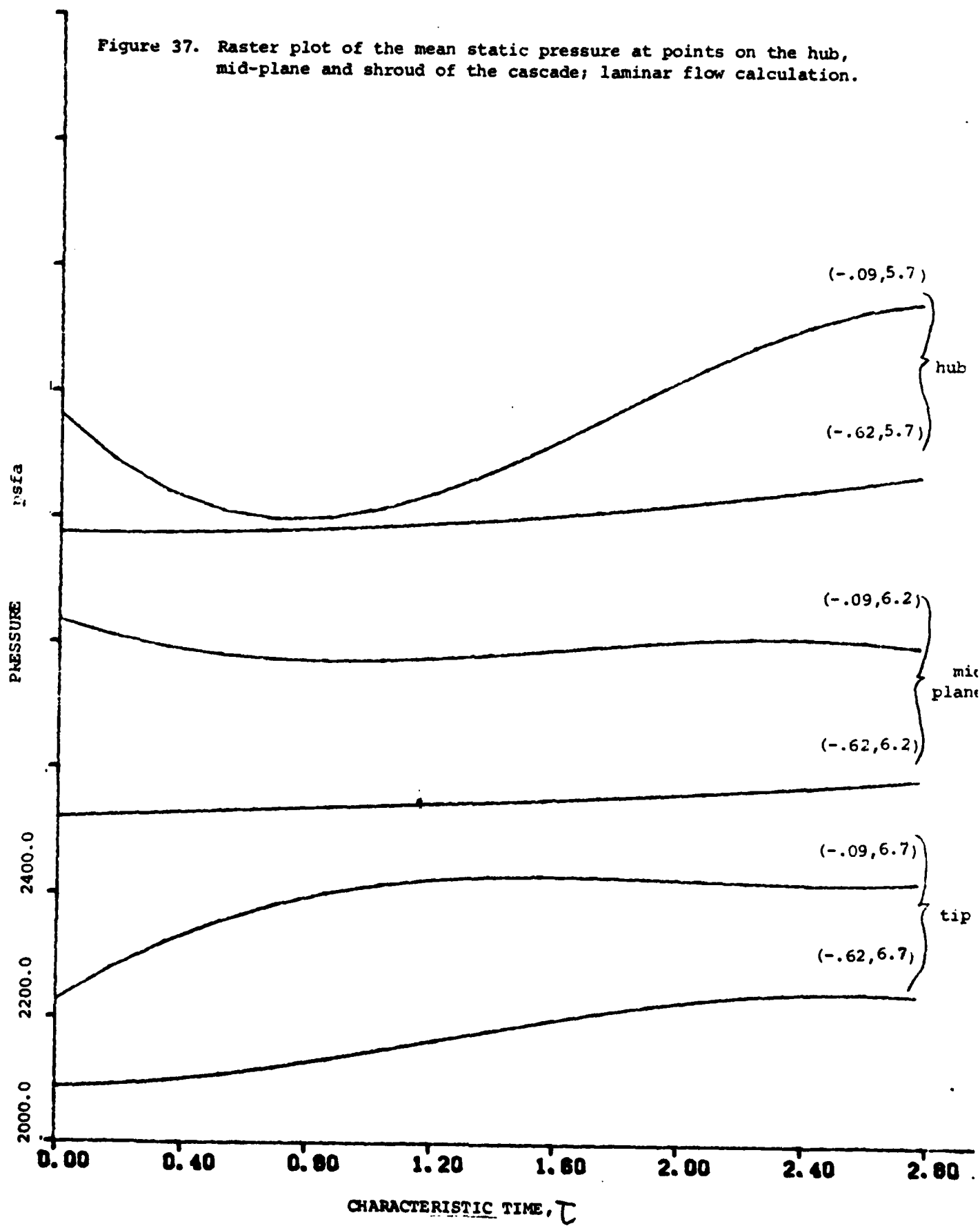
70

Figure 38. Raster plot of the static pressure fluctuation at points on the hub, mid-plane and shroud of the cascade; laminar flow calculation.
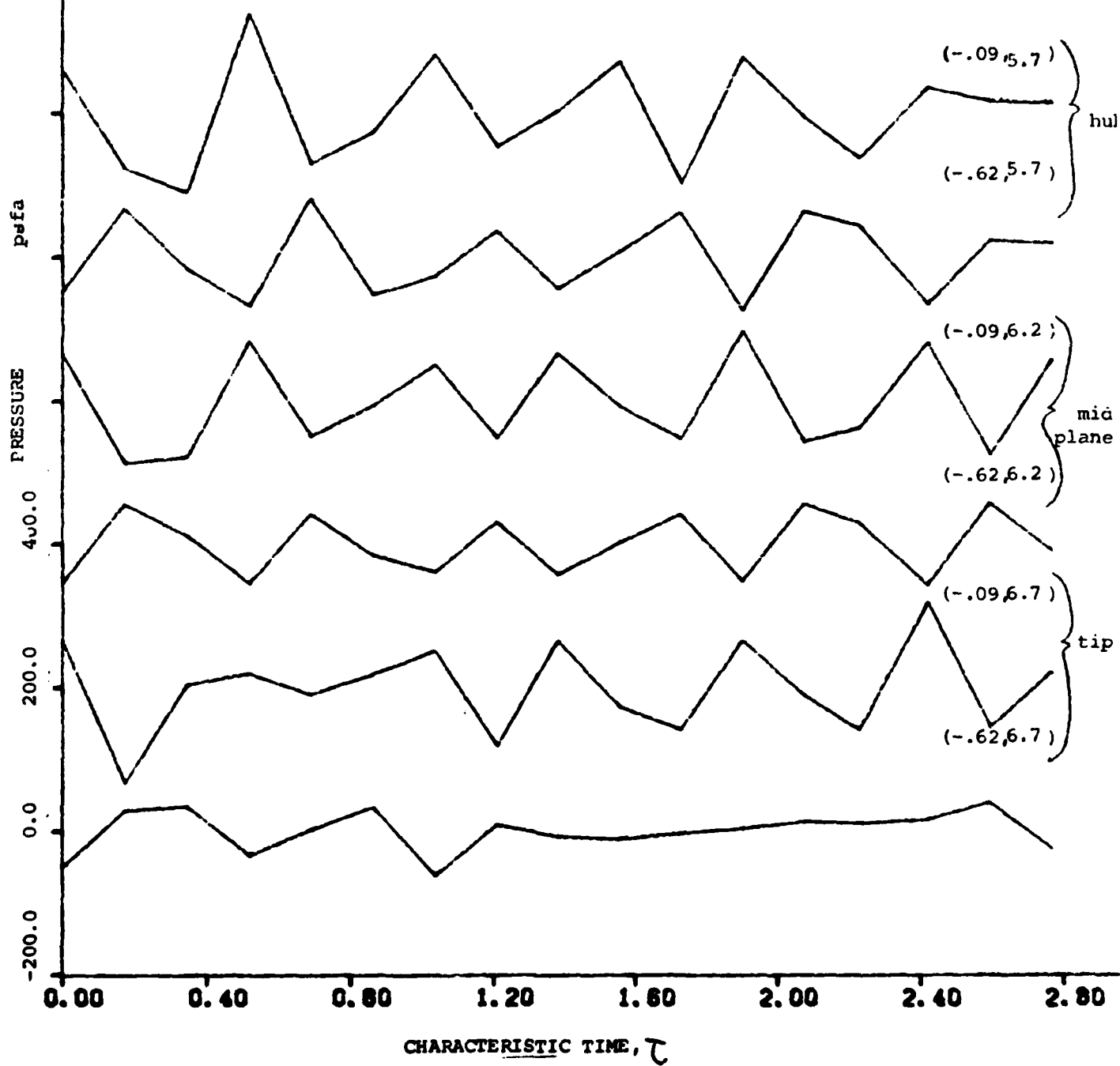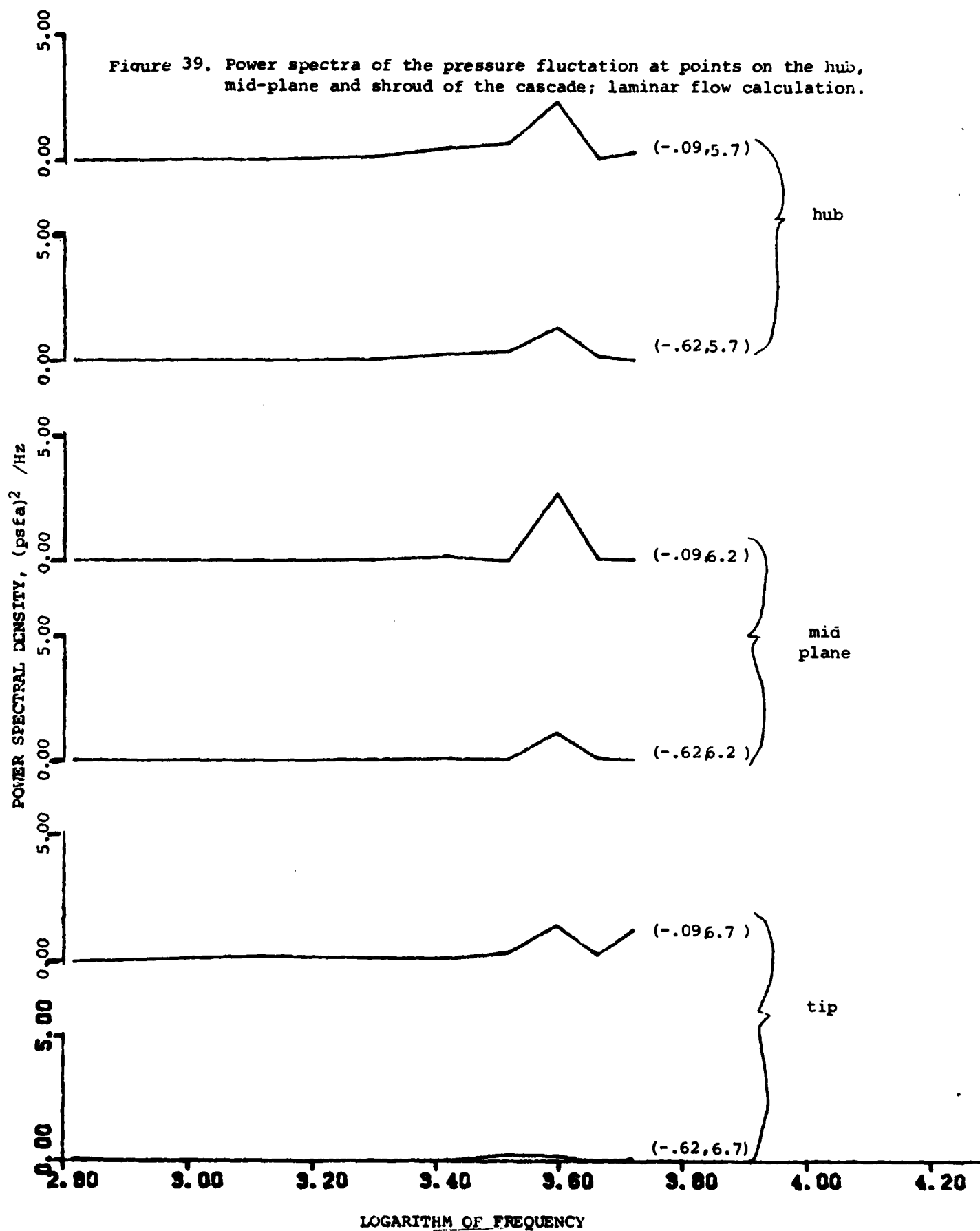
71

Figure 39. Power spectra of the pressure fluctation at points on the hub, mid-plane and shroud of the cascade; laminar flow calculation.
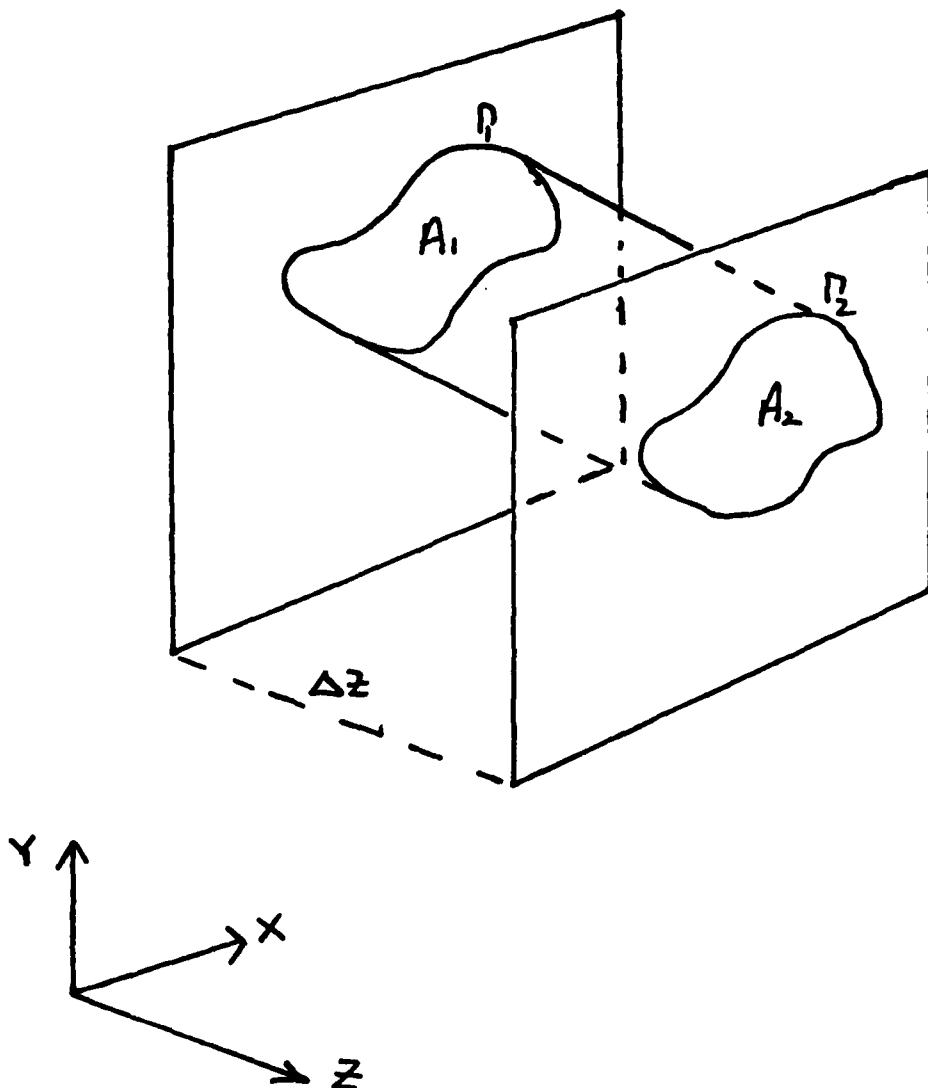
Figure 40.   Eulerian Cartesian Coordinate System (x,y,z)
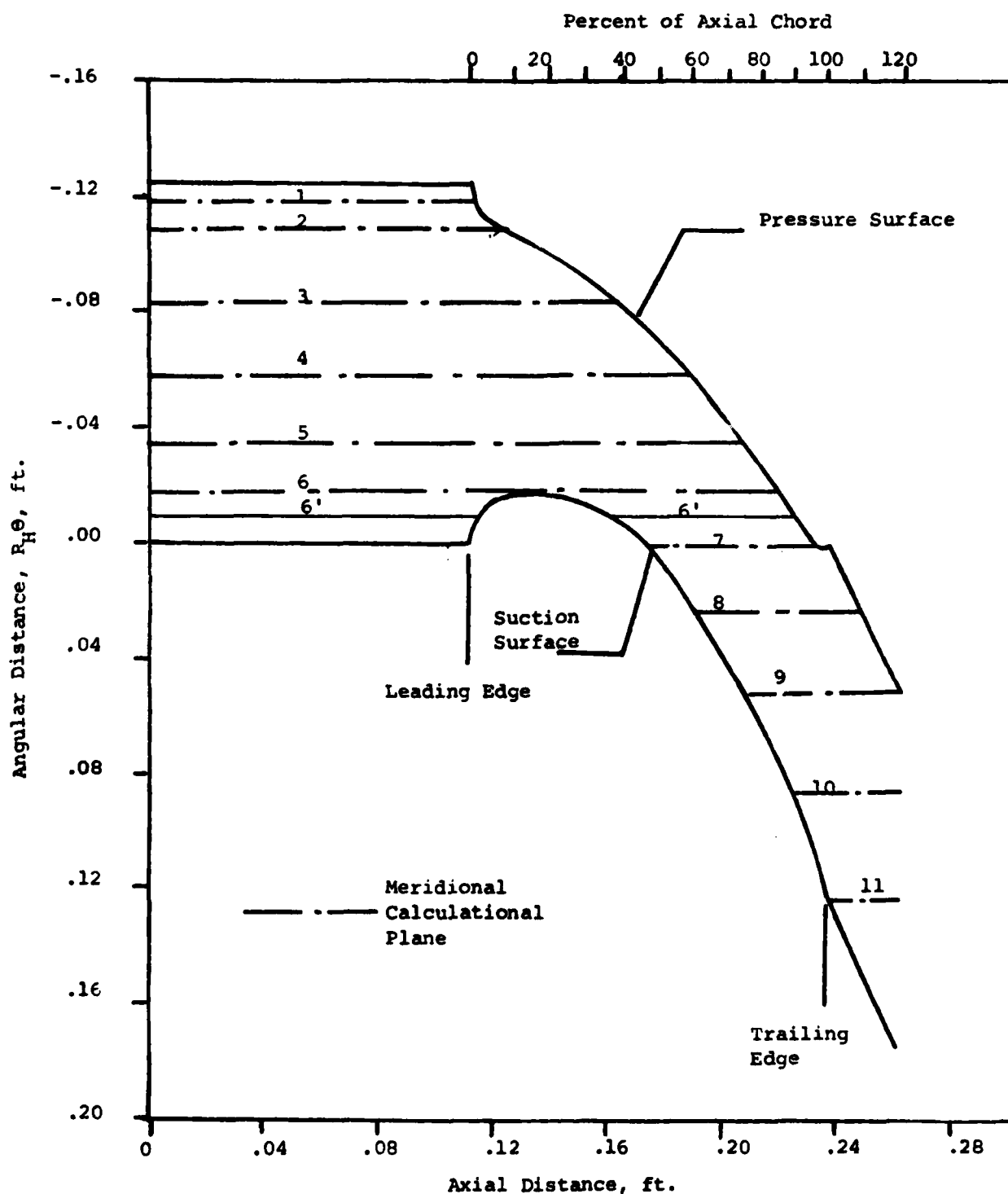
Figure 41. Hub Blade-to-Blade Surface Showing Preliminary Locations of Calculational Meridional Planes; R_H = .7083 ft.

74

1. Report No. NASA CR-168275 USAAVSCOM-TR-84-C-3	2. Government Accession No. AD-A145641	3. Recipient's Catalog No.
4. Title and Subtitle Calculation of the 3-D Viscous Flow at the Endwall Leading Edge Region of an Axial Annular Turbine Cascade		5. Report Date August 1984
		6. Performing Organization Code 505-40-4K
7. Author(s) Leonard Walitt		8. Performing Organization Report No. SR38
		10. Work Unit No.
9. Performing Organization Name and Address Thermo Mechanical Systems Company 7957 Alabama Avenue Canoga Park, California 91304		11. Contract or Grant No. DAAK51-81-C-0047
		13. Type of Report and Period Covered Technical Memorandum
12. Sponsoring Agency Name and Address U.S. Army Research & Technology Laboratories (AVSCOM) Propulsion Laboratory, Lewis Research Center, Cleveland, Ohio 44135 and NASA Lewis Research Center, Cleveland, Ohio 44135		14. Sponsoring Agency Code 1L161101AH45

15. Supplementary Notes

Final report. Project Manager, Kestutis C. Civinskas, Propulsion Laboratory, AVSCOM Research and Technology Laboratories, Lewis Research Center, Cleveland, Ohio 44135.

16. Abstract

A three-dimensional viscous computer code (VANS/MD) was employed to calculate the turbulent flow field at the end wall leading edge region of a 20 inch axial annular turbine cascade. The initial boundary layer roll-up and formation of the end wall vortices were computed at the vane leading edge. The calculated flow field was found to be periodic with a frequency of approximately 1600 Hz. The calculated size of the separation region for the hub endwall vortex compared favorably with measured endwall oil traces. In an effort to determine the effects of the turbulence model on the calculated unsteadiness, a laminar calculation was made. The periodic nature of the calculated flow field persisted with the frequency essentially unchanged. *Additional author assigned Keywords Include:*

17. Key Words (Suggested by Author(s)) Axial flow turbines; Viscous flow; Three-dimensional flow; Secondary flow; Vortices, (2nd)	18. Distribution Statement Unclassified - unlimited STAR Category 02		
19. Security Classif. (of this report) Unclassified	20. Security Classif. (of this page) Unclassified	21. No. of pages 76	22. Price* A05

75

END

FILMED

10-84

DTIC